PASJ: Publ. Astron. Soc. Japan **55**, 789–800, 2003 August 25

Dusty ERO Search behind Two Massive Clusters

Tadafumi TAKATA,[1] Nobunari KASHIKAWA,[2] Kouichiro NAKANISHI,[3]
Kentaro AOKI,[1] Ryo ASAI,[2] Noboru EBIZUKA,[5] Motoko INATA,[4] Masanori IYE,[2]
Koji S. KAWABATA,[2] George KOSUGI,[1] Youichi OHYAMA,[1] Kiichi OKITA,[4]
Toshiyuki SASAKI,[1] Yoshihiko SAITO,[2] Kazuhiro SEKIGUCHI,[1] Yasuhiro SHIMIZU,[4]
Hiroko TAGUCHI,[2] and Michitoshi YOSHIDA[4]

[1]*Subaru Telescope, National Astronomical Observatory of Japan, 650 North A'ohoku Place, Hilo, Hawaii 96720, U.S.A.*
takata@naoj.org

[2]*Opt/IR Astronomy Division, National Astronomical Observatory, 2-21-1 Osawa, Mitaka, Tokyo 181-8588*

[3]*Nobeyama Radio Observatory , National Astronomical Observatory, 462-2 Nobeyama, Minamimaki, Minamisaku, Nagano 384-1305*

[4]*Okayama Astrophysical Observatory , National Astronomical Observatory, Kamogata, Asakuchi, Okayama 719-0232*

[5]*RIKEN (The Institute of Physical and Chemical Research), 2-21 Hirosawa, Wako, Saitama 351-0198*

(Received 2002 December 7; accepted 2003 June 10)

Abstract

We performed deep K'-band imaging observations of 2 massive clusters, MS 0451.6−0305 at $z = 0.55$ and MS 0440.5+0204 at $z = 0.19$, for searching counterparts of the faint sub-mm sources behind these clusters, which would provide one of the deepest extremely red object (ERO) samples. Comparing our near-infrared images with optical images taken by the Hubble Space Telescope and by the Subaru Telescope, we identified 13 EROs in these fields. The sky distributions of EROs are consistent with the previous results, that there is a sign of strong clustering among detected EROs. Also, the surface density with corrected lensing amplification factors in both clusters are in good agreement with that derived from previous surveys. We found 7 EROs and 3 additional very red objects in a small area ($\sim 0.6\,\mathrm{arcmin}^2$) of the MS 0451.6−0305 field around an extended SCUBA source. Many of their optical and near-infrared colors are consistent with dusty star-forming galaxies at high redshifts ($z \sim 1.0$–4.0), and they may be constituting a cluster of dusty starburst galaxies and/or lensed star-forming galaxies at high redshift. Their red $J - K'$ colors and faint optical magnitudes suggest they are relatively old massive stellar systems with ages (> 300 mega years) suffering from dust obscuration. We also found a surface-density enhancement of EROs around the SCUBA source in the MS 0440.5+0204 field.

Key words: galaxies: clusters: individual (MS 0451.6−0305, MS 0440.5+0204) — galaxies: evolution — galaxies: high-redshift — galaxies: individual (SMM J04542−0301, SMM J04541−0302)

1. Introduction

Following the commissioning of SCUBA on JCMT (Holland et al. 1999), sub-mm surveys of distant universe have rapidly increased the number of sub-mm selected galaxies (Hughes et al. 1998; Eales et al. 1999; Barger et al. 1998; Smail et al. 1997, 2002a; Chapman et al. 2002a; Fox et al. 2002; Scott et al. 2002). The advantages of selecting high redshift objects based on a sub-mm wavelength are not only their negative k-correction up to $z \sim 10$ (Blain et al. 2002) but also their high sensitivity to very dusty objects, which are believed to be undergoing vigorous star formation at high redshift [their median redshift is revealed to be ~ 2.4 (Smail et al. 2002a; Chapman et al. 2003)]. They are one of the candidates of forming giant elliptical galaxies based on the current observational and theoretical predictions (Lilly et al. 1999). Although a very limited number of optical counterparts have been identified spectroscopically, they show notable diversity in their morphology (extended and/or merging), AGN possessions, dust temperatures, and so on (Smail et al. 2002a). To study the mechanisms of galaxy formations, such as merging and/or gravitational collapses, we need to clarify the nature and the environments of these faint sub-mm sources. Clearly, we need a much larger sample of faint sub-mm sources than we currently have. It also helps for comparing their features with nearby analogous objects, such as ultra-luminous IRAS galaxies and/or some other dusty populations detected by ISO, MAMBO, etc. These populations might be missed by the popular "Lyman break galaxy surveys" [there are only few cases of Lyman break galaxies with sub-mm detection (e.g. Chapman et al. 2002c)]. On the other hand, as firstly reported by Cimatti et al. (1998), there is some evidence that many of the sub-mm sources are associated with EROs (extremely red objects) (Cimatti et al. 1998; Blain et al. 2002; Smail et al. 2002a; Ivison et al. 2002; Wehner et al. 2002; Frayer et al. 2003). EROs have red colors, which is consistent with elliptical galaxies at high redshift, and they are separated into two categories of dusty starburst population and passively evolved stellar systems. The former are believed to be young high redshift objects with a large star-formation rate, and their features are consistent with forming elliptical galaxies based on theoretical predictions. Therefore, searching for EROs associated with faint SCUBA sources is one of the most effective methods for detecting obscured (dusty) star-forming galaxy at high redshift, though it may be limited only for $z \leq 3$, because of large extinction of their optical (rest UV) light by their

internal dust. There have been several studies (Smail et al. 1999; Ivison et al. 2000; Frayer et al. 2000; Barger et al. 2000; Lutz et al. 2001; Frayer et al. 2003) which identified the ERO counterparts of the sub-mm sources. Furthermore, Ivison et al. (2000) succeeded to obtain the redshifts of SCUBA sources at $z \sim 2.56$ and $z \sim 2.2$ in the A 1835 region, and there are some lower redshift samples with spectroscopically determined redshifts (e.g. Smith et al. 2001). The lack of a suitable sample is partly because of their optical faintness. Thus, it is needed to search for ERO counterparts to those sub-mm sources that are optically bright enough for detailed spectroscopic studies.

Using the gravitational lensing effect as a natural telescope, which amplifies the brightness of distant objects behind the lens, is one of the most powerful methods for obtaining detailed information on intrinsically faint objects. There have been many successful results in observing various types of high redshift galaxies using this effect, such as Lyman break galaxies (Pettini et al. 2000; Franx et al. 1997), faint SCUBA sources (Ivison et al. 2000, 2001; Ledlow et al. 2002), and EROs (G.P. Smith et al. 2002). The advantages of using the lensing effect is not only its photometric, but also spatial magnification, which will provide enlarged images of smaller distant objects, corresponding to a very high effective spatial resolution, which could not be achieved by the usual ground based observations. By using these effects, we could investigate the detailed structures and also the environmental status of distant objects.

In order to search for bright counterparts of SCUBA sources and to investigate their surrounding environments in detail, we performed ERO search observations behind two massive clusters of galaxies, MS 0451.6−0305 ($z = 0.55$) and MS 0440.5+0204 ($z = 0.19$). These clusters were discovered in the Einstein Medium Sensitivity Survey (EMSS) (Gioia et al. 1990), and were covered by a SCUBA mapping observation by Chapman et al. (2002a) and Smail et al. (1998; 2002a).

In the next section, we describe our data collection, including our observations. In section 3, we address the result of our imaging surveys and the various features of the candidates of the SCUBA source counterparts. A discussion is given in section 4. In this paper we use the cosmological parameters $H_0 = 60.0\,\mathrm{km\,s^{-1}\,Mpc^{-1}}$, $\Omega_\mathrm{M} = 0.3$, and $\Omega_\Lambda = 0.7$. All magnitudes without any notice are given in Vega magnitude. We used the values in Fukugita et al. (1996) for converting between the AB and Vega scale magnitudes.

2. Observation, Data, and Data Reduction

2.1. Optical Data

2.1.1. HST data

Deep optical imaging data for both clusters taken by WFPC2 through a F702W filter were retrieved from the HST archive system[1] at STScI. The total exposure times for each cluster were 10400 seconds for MS 0451.6−0305 (Program ID 5987) and 22200 seconds for MS 0440.5+0204 (Program ID 5402), respectively. We used a post-calibrated data and combined them into one image by a drizzling technique implemented in 'dither' package in STSDAS, running in the IRAF[2] environment (Fruchter, Hook 2002). The depths for both images are 26.3 and 26.6 ST-mag (R_ST) (assuming $2''$ diameter aperture with 2σ detection), respectively.

2.1.2. Optical imaging with Subaru Telescope

Optical imaging using Kron–Cousin's R_c and I_c band filters for complementing WFPC2 data were performed for MS 0451.6−0305 using the Faint Object Camera and Spectrograph (FOCAS) (Kashikawa et al. 2002) at the Cassegrain focus of Subaru Telescope on 2000 December 29, during a commissioning observation run of FOCAS. Johnson B and SDSS z' imaging observations were performed on 2002 November 1 and 2, using Subaru Prime Focus Camera (SuprimeCam) (Miyazaki et al. 2002) attached to the prime focus of the Subaru telescope. All these images, except for z'-band image, were taken under good photometric conditions. The total exposure times were 3600, 1800, 1800, and 2940 s for the B, R_c, I_c, and z'-bands, respectively. We applied the standard calibration for these data using IRAF tasks for the FOCAS data, and the software package for SuprimeCam data (Yagi et al. 2002). Photometric calibrations were performed using "RUBIN 152" in Landolt's standard stars catalog (Landolt 1992) for the FOCAS data, and SA 95 for the SuprimeCam data (J.A. Smith et al. 2002). The limiting magnitudes of the images were 27.3, 25.6, 24.5, and 24.6 mag for the B, R_c, I_c, and z'-bands, respectively, for 1σ detection within $2''$ diameter. Photometric errors for each band were estimated as being equal or less than 0.1 mag, except for the z'-band (~ 0.2). For a z' photometric calibration, we used images taken by HST/ACS through F850LP filter, and confirmed the accuracy of our photometry to be less than 0.2 mag. We used the STSDAS synphot package to convert from F850LP mag to z' mag. The seeing sizes were $0\farcs6$, $0\farcs6$, $0\farcs55$, and $0\farcs7$ for the B, R_c, I_c, and z' bands respectively.

We also retrieved Johnson V image taken by SuprimeCam with 3600 s exposure from SMOKA (Subaru Mitaka Okayama Kiso Archive system)[3] (Baba et al. 2002), and reduced it in the standard manner. We performed a photometric calibration using standard stars in SA 95 and SA 107 (Landolt 1992), and estimated the limiting magnitude ($2''$ aperture with 1σ) to be 26.7. We checked the catalog with published V mag data of the same field (Stanford et al. 2002), and estimated the errors to be within 0.1 mag.

2.2. Near-Infrared Imaging

K'-band imaging observations were performed on 2000 November 17 and 18, and J-band imaging observation was made on 2002 January 6, using the Cooled Infrared Spectrograph and Camera for OHS (CISCO) (Motohara et al. 2002) attached to the Nasmyth focus of Subaru Telescope. Both clusters' images were taken by using 8 point dithering of 12 exposures with 20 s each for the K'-band and of 6 exposures

[1] Based on observations made with the NASA/ESA Hubble Space Telescope, obtained from the data archive at the Space Telescope Science Institute. STScI is operated by the Association of Universities for Research in Astronomy, Inc. under NASA contract NAS 5-26555.

[2] IRAF is distributed by the National Optical Astronomy Observatories, which are operated by the Association of Universities for Research in Astronomy, Inc., under cooperative agreement with the National Science Foundation.

[3] ⟨http://smoka.nao.ac.jp/⟩.

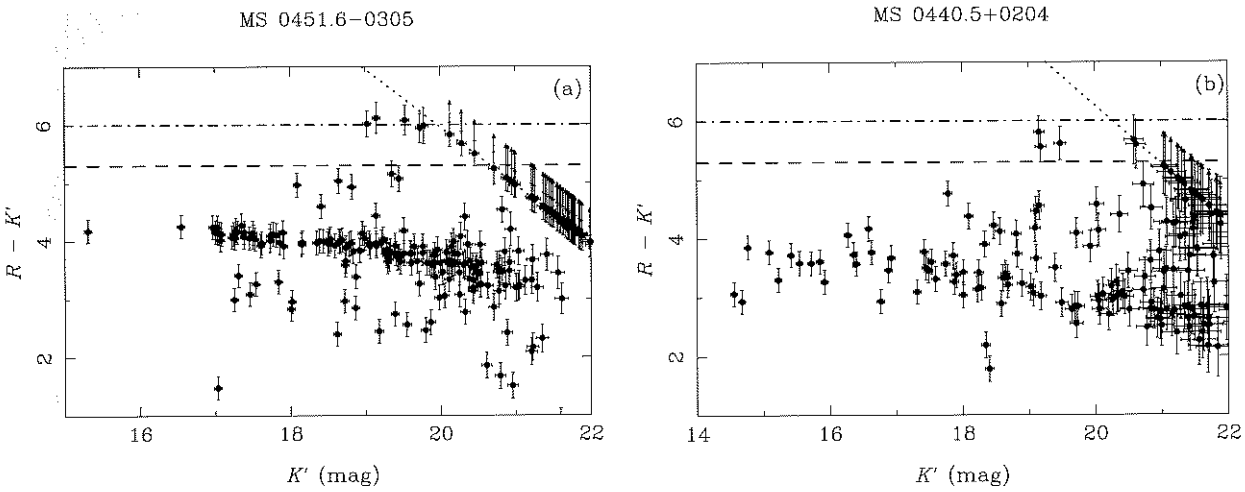

Fig. 1. (a) K' vs $R_c - K'$ plot for MS 0451.6−0305. Color of $R_c - K' = 5.3$ and 6.0, which represent those for EROs, are shown by the dashed and dash-dotted line, respectively. The line indicating the 2σ limit of the R_c-band image is also shown. (b) Same figure for MS 0440.5+0204.

with 40 s for the J-band, covering about a $2'.0 \times 2'.0$ field of view. The total exposure times were 9220 s in the K'-band, and 3600 s in the J-band for MS 0451.6−0305 and 6880 s in the K'-band for MS 0440.5+0204. The seeing sizes were $0''.6$ to $0''.8$ in the K'-band, and $0''.7$ to $0''.9$ in the J-band. The sky conditions were mostly photometric during the observation in 2000 November, but not on 2002 January 6. We used FS 10 and FS 12 from the UKIRT faint standard catalog (Casali, Hawarden 1992) for photometric calibrations. The depth of our observations reached to 22.1 mag in K' and 22.3 mag in J with 1σ detection within $2''$ diameter. For K', we estimated the errors in our photometry to be less than 0.1 mag, but we could not confirm the error for the J-band using our data set, because it was not taken under photometric condition. Therefore, we compared the J-band mag of our sample with those of a somewhat shallower sample by Stanford et al. (2002) with a limiting magnitude of about 20.5, and found no systematic difference between these two datasets (less than 0.1 mag in r.m.s.).

Astrometric calibrations were performed using USNO-A2.0 catalog in each field. For MS 0451.6−0305, we used the B-band SuprimeCam image for obtaining a wider field of view and about 900 stars with r mag between 16 to 18 for fitting (for avoiding the position measurement error by saturation). After the fitting, we applied the measured positions of objects in the CISCO K' image and refit them. We used the HST F702W image for MS 0440.5+0204 with 10 stars, because it is the widest image for this field. The resultant r.m.s. in the fittings were $0''.20$ and $0''.36$ for MS 0451.6−0305 and MS 0440.5+0204, respectively.

3. Results

3.1. Sample Extraction and Completeness

We used SExtractor (Bertin, Arnouts 1996) for making the K'-band selected catalog, which reached to a depth of ~ 22.1 mag in $2''$ diameter aperture. An eye inspection was also carried out for all extracted sources, and spurious sources were eliminated from the sample. Photometry of other bands' images was carried out using the "double image mode", based on the K'-band image. For obtaining precise color information, we applied Gaussian smoothing to B, V, F702W, R_c, I_c, z', and K' frames for matching the image qualities to that of the J-band, which had the worst seeing size. We set the detection criteria at 15 contiguous pixels ($0''.105\,\mathrm{pix}^{-1}$) exceeding 1.5σ levels, and detected 235 and 164 objects with $K' \leq 22.0$ for MS 0451.6−0305 and MS 0440.5+0204, respectively. The following results and discussions are based on the magnitudes with $2''$ diameter photometry, which corresponds to a linear scale of about 7 kpc and 15 kpc for $z = 0.19$ and 0.55, respectively.

The completeness of our catalog was estimated by adding artificial objects to the K' images for each field at empty positions. We used the IRAF package artdata for simulating and adding point-like sources as well as objects with de Vaucouleurs and exponential profiles (convolved with the seeing PSF) onto the images. SExtractor was run with the same detection parameters as for the real data. The limiting magnitudes with 80% completeness for each field were 21.5 for MS 0451.6−0305, and 21.7 for MS 0440.5+0204, respectively, using point sources, and they decreased to about 65% for objects with exponential profiles at these magnitudes. The completenesses at $K' = 22.0$ of point-source detection were $\sim 50\%$ and $\sim 60\%$, respectively for MS 0451.6−0305 and MS 0440.5+0204.

We adopted the photometric system from Holtzman et al. (1995) for deriving the R_c-band mag from the HST F702W-band data, which are suitable for comparing the previous ERO surveys. We assumed the color of Sbc galaxies at a redshift of $z = 1$–2 ($V - R \sim 1.1$), which is the same manner of transformation adopted by G.P. Smith et al. (2002). The systematic uncertainty of this conversion is ≤ 0.1, which arises from the likely presence of both more and less evolved galaxies than the adopted Sbc spectral type. We independently checked the observed FOCAS R_c-band mag with these transformed magnitudes for the same objects, and confirmed the consistency with

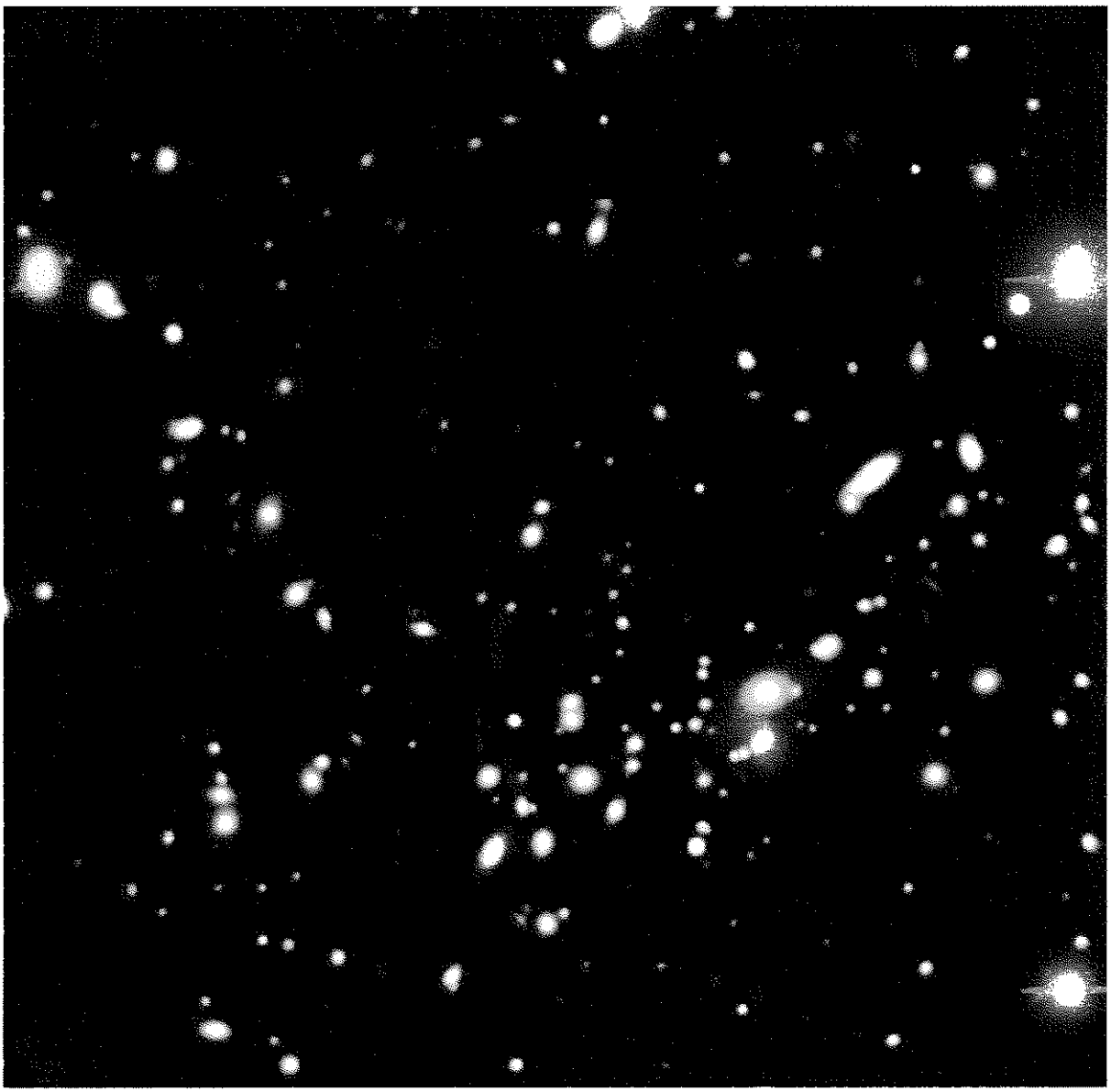

Fig. 2. Three-color $R_c I_c K'$ image of MS 0451.6−0305 (using R_c and I_c data by FOCAS and a K' image by CISCO). This is a $2' \times 2'$ field of view. We identify several very red objects mainly detected in K' image.

each other. In the following discussions, we use the R_c-band mag which were transformed from the F702W mag.

Figure 1 shows a K' vs $R_c - K'$ diagram for the 2 fields with lines of $R_c - K' = 5.3$ and 6.0, which are our used ERO selection criteria. Most of the objects are concentrated around $R_c - K' \sim 3$–4, which is consistent with the color of early-type galaxies of cluster members at the corresponding redshifts and is also consistent with the results of shallower observations by Stanford et al. (1998) for MS 0451.6−0305.

There are 2(8) EROs in the MS 0451.6−0305 region with $R_c - K' \geq 6.0\,(5.3)$, and the number density is $0.5\,(2.0)\,\mathrm{arcmin}^{-2}$ down to $K' = 20.8$ [it is the limit of $R_c - K' > 5.3$ with $R_c < 26.1$ ($R_{ST} < 26.5$) sample], simply dividing the surveyed area ($4\,\mathrm{arcmin}^2$) without any correction for lens amplification. When limiting the magnitude with $K' = 20.0$, the numbers are reduced to 2 (5). For MS 0440.5+0204, there are 0 (5) EROs with $R_c - K' \geq 6.0\,(5.3)$, and the uncorrected number density is $0.0\,(1.25)\,\mathrm{arcmin}^{-2}$ down to $K' = 21.0$. When limiting the magnitude with $K' = 20.0$, the numbers are reduced to 0 (3).

Figure 2 shows three-color (R_c, I_c, K') image of MS 0451.6−0305 with $2' \times 2'$ field of view. There are some red objects which are bright in the K' band. Figure 3 shows the sky distributions of EROs in MS 0451.6−0305 and MS 0440.5+0204, respectively for showing clustering properties in each field. It is clear that both in the MS 0451.6−0305 and the MS 0440.5+0204 regions, there is a non-uniform trend in the sky distribution of EROs and clustering in southern part of MS 0451.6−0305, while near the image center in MS 0440.5+0204.

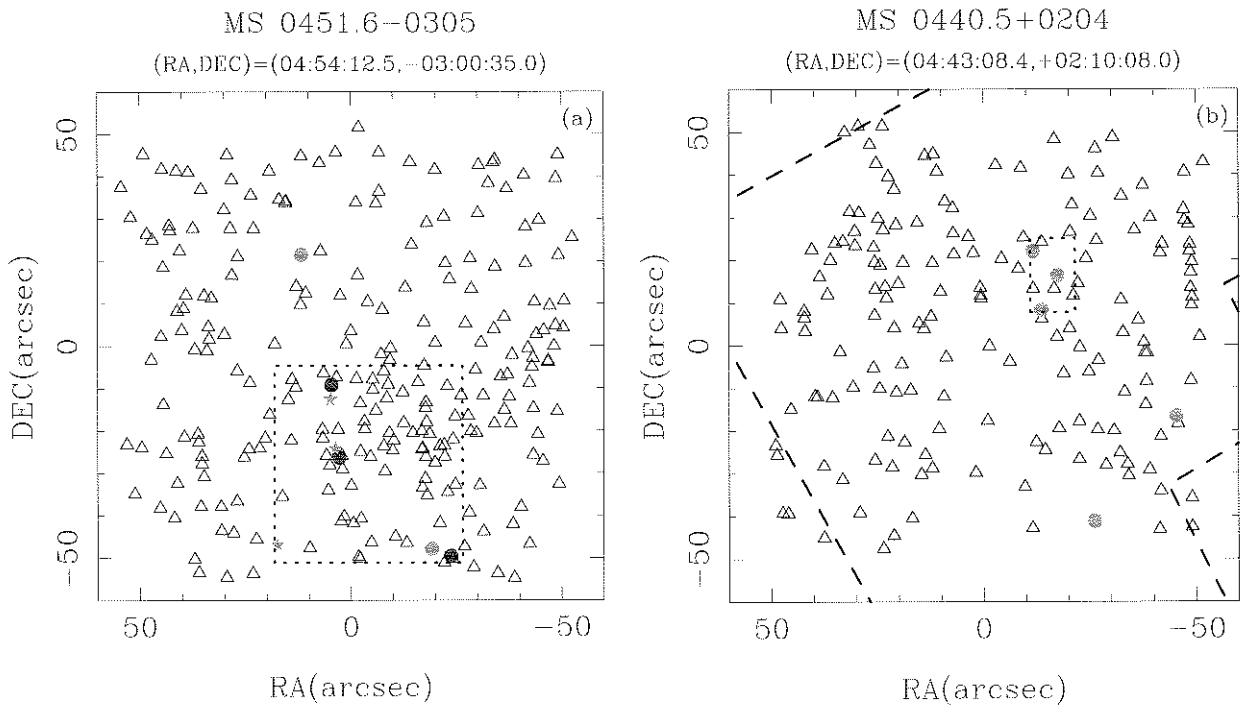

Fig. 3. Sky distributions of EROs in the regions of (a) MS 0451.6−0305 and (b) MS 0440.5+0204. Darkfilled circles, half-tone filled star, half-tone filled circles represent ERO with $R_c - K' \geq 6.0$, ones with $5.3 \leq R_c - K' \leq 6.0$ with and without upper limit value of R_c mag, respectively. Triangles represent other sources detected in K'-band image for those fields. Regions encircled by dotted lines are showing the area we used for surface density calculations. The dashed line in (b) is showing the edge of F702W image. Central coordinates in J2000.0 for both fields are denoted at the top of the panels.

3.2. *Counterparts of SCUBA Sources*

3.2.1. *SCUBA sources in MS 0451.6−0305*

Two sub-mm sources, SMM J04542−0301 and SMM J04541−0302, were detected in a survey of massive clusters using SCUBA by Chapman et al. (2002a).

SMM J04542−0301 is located at 25″ from the cluster center, and elongated to about 1′ long, which is suggested to be a blend of multiple SCUBA sources (Chapman et al. 2002a). Its total flux at 850 μm is 19.1 mJy, and the magnification factor by cluster lensing is estimated to be 4.5. There is a constraint of the redshift for this source, as at $z \geq 2.3$ using the 'sub-mm' vs 'cm' spectral index (Yun, Carilli 2002). We found 7 EROs and 3 optically bright ($R_c \sim 23$–24) very red objects ($R_c - K' \sim 5$) around this sub-mm source, as shown in figure 4. The photometric parameters for these objects are summarized in table 1. "A1" and "A4" are very faint, even in a very deep (10400 s exposure) F702W image, and "A2" and "A3" are not visible in it. We plot $R_c - K'$ vs $J - K'$ diagrams to perform the diagnostics for distinguishing dusty star-forming EROs from passively evolved ones, as suggested by Pozzetti and Mannucci (2000) for identifying more plausible counterpart of the SCUBA source among those EROs in figure 5, in case they are at $1 < z < 2$. We also plotted the color tracks of elliptical and dusty starburst galaxies based on the GISSEL 99 model (Bruzual, Charlot 1993) for calculating the SEDs of each track. The ellipticals are represented by a simple stellar population with solar metallicity with Salpeter IMF with an age of 15 Gyr. For dusty starbursts, we used a model with a constant star formation rate over 1Gyr reddened to $E(B-V) = 0.8$ using the dust-extinction law by Calzetti et al. (2000). We used the criteria suggested by Pozzetti and Mannucci (2000) for distinguishing two populations of EROs, which is $(J-K) = 0.34(R-K) + 0.19$ with $R_c - K > 5.3$, and found that more than half of the EROs near the SCUBA source ("A1", "A4", "E", and "F") can be categorized as dusty starburst populations. They may consist of groups of dusty EROs or some blends of lensed objects, because "A1" to "A4" are well aligned along another arc, which is denoted as "Blue Arc" in figure 4. It should be noted that if many of those EROs do not inhabit at $1.0 < z < 2.0$ this diagnostics are not very effective, because there will be overlaps of the occupation area between two classes of objects in color–color spaces. For higher redshift objects, it is suggested to use $J - K$ vs $H - K$ diagram in Pozzetti and Mannucci (2000). We could not perform this diagnostic because of a lack of H-band information for our sample. More detailed discussions will be given in the next section.

SMM J04541 − 0302 is unresolved in the SCUBA map at 65″ from the cluster center, and lens amplification factor is 2.6 (Chapman et al. 2002a). The flux at 850 μm is 16.8 mJy, and the constraint on photometric redshift derived from radio index is $z \geq 2.2$. Since this source is out of the field of view of our J and K' images, we can search for a counterpart only in optical B, V, R_c, I_c, and z' images taken by FOCAS and SuprimeCam. In these images, a relatively bright galaxy, with

Table 1. Photometric properties of EROs and red objects around SMM J04542 − 0301.*

Name	RA (J2000)	DEC	Magnitudes ($2''$ aperture) and colors								
			K'	B	V	R_c	I_c	z'	J	$R_c - K'$	$J - K'$
A1	04:54:12.81	−03:00:44.2	19.1	27.2†	26.3†	25.1†	> 24.5	24.4†	> 22.3	6.0	> 3.2
A2	04:54:12.82	−03:00:47.6	20.1	> 27.3	> 26.7	> 26.0	> 24.5	> 24.6	> 22.3	> 5.9	> 2.2
A3	04:54:12.74	−03:00:59.2	20.5	24.6‡	23.6‡	> 26.0	> 24.5	21.2‡	> 22.3	> 5.5	> 1.8
A4	04:54:12.68	−03:01:01.3	19.0‡	> 27.3	26.3‡	25.4‡	24.4‡	23.7‡	22.1‡	6.4	3.1
A4($1''\phi$)			19.8‡	> 28.8	27.9‡	26.1‡	25.3‡	24.8‡	23.0‡	6.3	3.2
B	04:54:13.43	−03:00:42.9	19.4‡	27.3‡	25.5‡	24.5‡	23.6‡	23.2‡	22.0‡	5.1	2.6
B($1''\phi$)			20.1	28.4	26.7	24.8	24.4	24.1	23.1	4.7	3.0
C	04:54:12.66	−03:01:16.3	18.6‡	26.2‡	24.6‡	23.7‡	22.8‡	22.4‡	21.6‡	5.1	3.8
C($1''\phi$)			19.3	27.8	26.0	24.2	23.6	23.4	22.7	4.9	3.4
D	04:54:12.33	−03:01:15.6	19.4	27.0	25.9	24.4	24.1	23.6	> 22.3	5.0	> 2.9
E	04:54:10.92	−03:01:24.5	19.5	27.1	26.0	25.6	> 24.5	> 24.6	> 22.3	6.1	> 2.8
F	04:54:11.22	−03:01:22.9	19.7	26.8	26.6	25.5	> 24.5	23.8	22.1	5.8	2.4
G	04:54:13.66	−03:01:21.9	20.3	> 27.3	> 26.7	> 26.0	> 24.5	> 24.6	> 22.3	> 5.7	2.0

* The upper limits indicate the 3σ detection level in each band. The magnitudes are given in the Vega scale. All of them are observed magnitudes, and were not corrected for the lensing effect.
† Possible another source.
‡ Possible contamination from other sources.

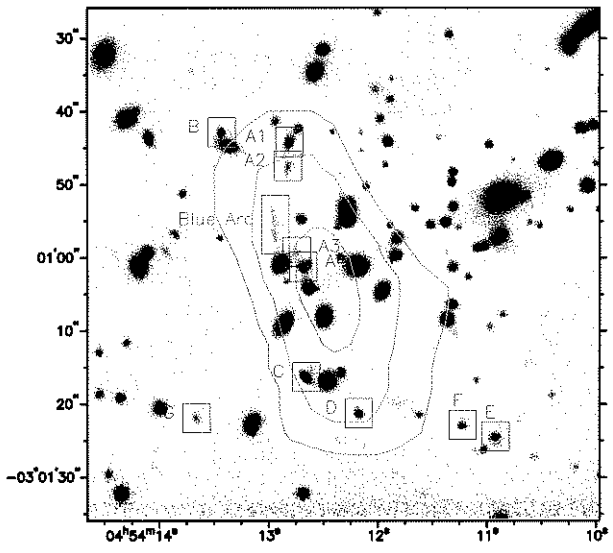

Fig. 4. K' image of the area around SMM J04542 − 0301 with an overplotted SCUBA contour map by Chapman et al. (2002a). The contour levels represent the 2σ to 4σ detection levels. EROs around the SCUBA source are represented as "A1" to "A4" and "E", "F", and "G" with red rectangles, and optically bright red objects ($R_c - K' \sim 5$) "B", "C", and "D" are also shown along with purple ones. The arc, which is clearly visible in the optical images, is denoted as "Blue Arc".

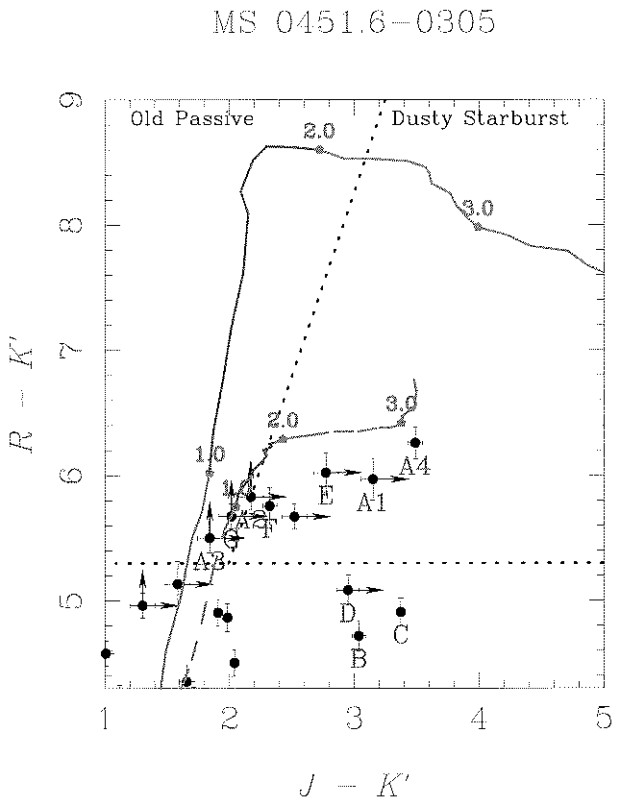

Fig. 5. $R_c - K'$ vs $J - K'$ diagram for the objects with red colors in the MS 0451.6−0305 region. The dotted lines indicate the boundary between passively evolved galaxies (left side) and dusty starbursts (right side) with an extremely red color ($R_c - K' = 5.3$). The objects which are identified near the extended SCUBA source are denoted as in figure 4. The curves indicate the track of elliptical galaxies (solid line) and dusty starbursts (dashed line) with a redshift range of 1 to 4 (redshifts 1.0, 2.0, 3.0 are denoted for each track). The details can be referred to in the text.

$R_c = 22.2$ with colors of $B - V = 1.3$, $B - R_c = 3.0$, $R_c - I_c = 1.0$, and $I_c - z' = 0.55$, is at nearly the SCUBA detection center. It has red colors, thus indicating a certain amount of dust obscuration. The SED fitting and photometric redshift estimate were carried out with hyperz (Bolzonella et al. 2000) with the information from these 5 bands. We had a fitting result with a dusty galaxy at low redshift (around $z \sim 0.6$) with $E(B - V) \sim 0.75$. It is a very possible counterpart for the sub-mm source, because it is believed to be suffering from large extinction by dust

Table 2. Parameters of clusters used in the lensing model.

Name	RA(J2000.0)	DEC(J2000.0)	z	σ_{los} (km s^{-1})	Reference	f
MS 0451.6−0305	04:54:10.8	−03:00:51.6	0.55	1354	Ellingson et al. (1998)	0.9
MS 0440.5+0204	04:43:09.9	+02:10:19.8	0.19	872	Gioia et al. (1998)	0.95

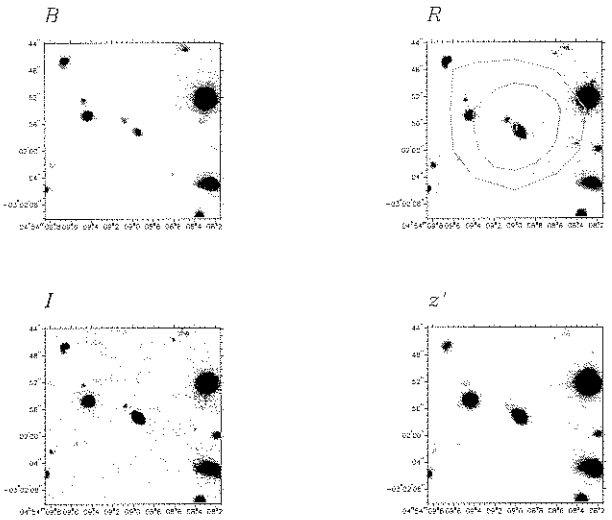

Fig. 6. FOCAS R_c and I_c bands and SuprimeCam B and z' images around SMM J04541−0302 in MS 0451.6−0305. The field sizes are $30'' \times 30''$. A contour map of SCUBA detection is overplotted on the R_c band image with the same levels as in figure 4.

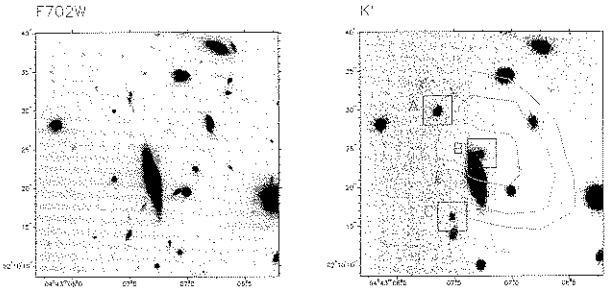

Fig. 7. F702W and K' images around SMM J04433 + 0210 in MS 0440.5+0204. EROs are denoted as "A", "B", and "C". "B" is the optical counterpart of the sub-mm source ("N4" in Frayer et al. 2003) at $z = 2.51$. Field sizes are $30'' \times 30''$. A bright galaxy neighboring "B" is "N1" in Smail et al. (1999). The overplotted contours in K' band image are 850 μm map in Smail et al. (1998).

(figure 6). This galaxy is already listed in the catalog of the CNOC cluster survey (Ellingson et al. 1998), and its r and g mag's are 22.53 and 24.23, respectively, without information about the redshift. Since there is no information on near-infrared nor radio wavebands for the objects, it is very difficult to identify a secure counterpart. The possibility of a sub-mm object lensed by a bright galaxy invisible in the optical bands, which was suggested by Chapman et al. (2002b), can not be eliminated.

3.2.2. *SMM J04433+0210 in MS 0440.5+0204*

SMM J04433+0210 was discovered in the "SCUBA Lens Survey" by Smail et al. (1997, 2002a), and its flux at 850 μm is 7.2 mJy. There is no detected radio flux for this source down to the 70 μJy level at 1.4 GHz (Smail et al. 2002a). An optical counterpart was reported by Frayer et al. (2003) as "N4", which was detected in their HST/F702W and K-band images. Their Keck spectroscopy revealed its redshift as being 2.51.

We measured the R_c mag for this object as 25.4 and 26.1 for $2''$ and $1''$ apertures, respectively, although there is a certain amount of contamination from the neighboring bright galaxy "N1", especially for a $2''$ aperture (figure 7). We also detected this object in the CISCO K' image ("B" in figure 7); the magnitudes are 19.5 and 20.3 for $2''$ and $1''$ apertures, respectively, which are in good agreement with the K mag in Smail et al. (1999) and Frayer et al. (2003). The estimated $R_c - K'$ color is 5.8 for $1''$ diameter magnitudes, and thus it is classified as EROs. It should be noted that there are two other EROs ("A" and "C") within $10''$ of the sub-mm source.

4. Discussions

4.1. *Lens Model and Surface Density Calculation*

As shown in figure 3 and figure 4, there are concentrations of EROs within a small area in both fields. For discussing the surface-density enhancement, it is not straightforward to compare our sample with other wide-field ERO surveys, because our observation is targeted to the fields of cluster of galaxies. The effects by gravitational lensing, such as amplification of the source flux and the accompanying distortion of the background sky (source plane), should be taken into account. In such a case, lensing models can be used to compute the lens amplification as a function of the image plane position.

We modeled lensing clusters using an elliptical potential with the parameters listed in table 2. The lensing inversion was based on the prescription of Kormann et al. (1994) and Schneider et al. (1992), allowing calculations of the lensing amplification and distortion as a function of the position in the image plane. The essential parameters of the model are the redshift and the line-of-sight velocity dispersion of the cluster. The cluster ellipticity (f in table 2) is chosen based on a measurement of each BCG (Brightest Cluster Galaxy) contour on the K'-band image.

The amplification imposed on each background galaxy depends on its redshift (z_{source}), and the redshift of the intervening lens (z_{lens}). We found that cumulative source counts depends weakly on the actual source redshift by investigating for the case of z_{source} = 1.2, 1.5, 2.0, 2.5, and 3.0, at which most of all EROs are expected to lie. Adopting a single value of z_{source} introduced an uncertainty of at most less than 40% into the final surface density values for the whole field of view in MS 0451.6−0305, while it was less than 20% for MS 0440.5+0204. For overcoming these uncertainties, we adopted two single source planes of z_{source} = 1.5 and 3.0, and

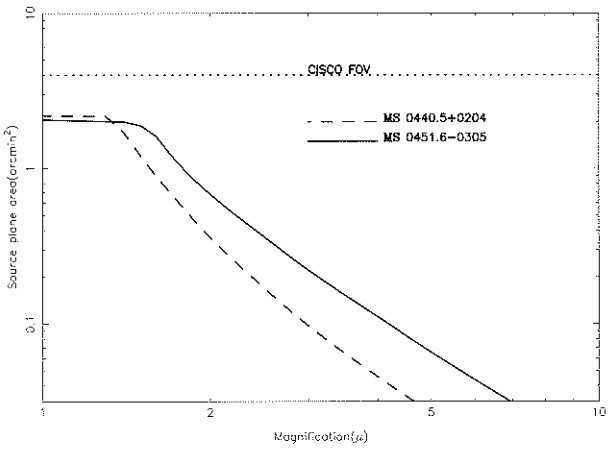

Fig. 8. Cumulative area of the source plane in our survey at $z = 1.5$ that experiences magnification greater than μ.

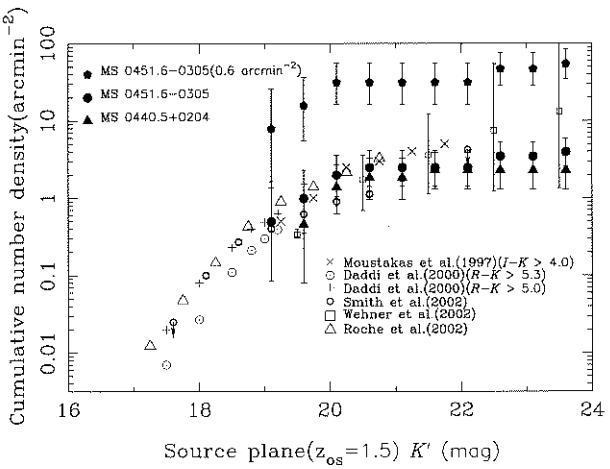

Fig. 9. Amplification-corrected surface densities of EROs for surveyed regions. The corrections were applied assuming a single source plane at $z_{source} = 1.5$, as discussed in the text. The triangles indicate the cumulative surface densities for MS 0440.5+0204, the filled pentagons and circles for MS 0451.6−0305 within a small region as shown in figure 3, and for the whole region, respectively. The open circles show the results of G.P. Smith et al. (2002), and the open squares represent those by Wehner et al. (2002). We also plotted the results of field ERO searches by Daddi et al. (2000), Moustakas et al. (1997), and Roche et al. (2002). We plotted them without any correction for the data with $R_c - K > 5.0$ or $I - K > 4.0$. The uncertainties for our data are 1σ, based on the Poisson distribution.

used in each cluster model to compute a map of the lens amplification as a function of the image plane position for each value of z_{source} in each cluster field.

We first used the amplification maps to de-amplify the image plane flux of each EROs in our sample, and hence obtain their source plane K'-band mag. Because gravitational lensing is achromatic, there is no need to correct the $R_c - K'$ color. The number of EROs that are brighter than a source plane limiting magnitude can then be found by simply counting the number of sources brighter than the limiting magnitude in the source plane after correcting for lensing. A simple Poisson uncertainty is attached to this value.

We then calculated the area of the background sky within which EROs were detectable in the relevant cluster field in the following manner. An ERO with a source plane magnitude of K'_{source} will appear in the image plane of the relevant cluster with a magnitude brighter than an image plane detection limit of K'_{det}, if it is magnified by a factor greater than $\mu_{min} = 10^{-0.4(K'_{det} - K'_{source})}$. The area in the source plane within which such a galaxy would be detected in that cluster is thus $A(\mu_{min})$, where $A(\mu_{min})$ is the area of the $z_{source} = 1.5$ source plane behind each cluster that lies within the CISCO field of view, and is magnified by a factor greater than μ_{min} (figure 8). Therefore, we can derive the surface number density from the dividing number of galaxies by $A(\mu_{min})$.

4.2. *Corrected Surface Density of EROs*

The derived surface densities for each cluster field are $2.43\,\mathrm{arcmin}^{-2}$ for $R_c - K' \geq 5.3$ in MS 0451.6−0305, and $2.29\,\mathrm{arcmin}^{-2}$ for $R_c - K' \geq 5.3$ in MS 0440.5+0204 at $K' = 21.6$ for the source plane at $z_{source} = 1.5$. The cumulative surface densities as a function of the K'_{source} mag for a sample with $R_c - K' \geq 5.3$ are shown in figure 9. We also plotted the result for the $0.6\,\mathrm{arcmin}^2$ area in MS 0451.6−0305 (rectangle surrounded by dotted lines in figure 3), in which 7 EROs were detected. About 20 and 10% of the whole survey areas reach to a depth of $K'_{lim} \sim 23.0$, when we adopt the detection limit as $K' = 22.0$. Because of the limit by the depth of the R-band mag, the depth of our "ERO samples" are decreased to $K_{source} \sim 22.0$. Our sample thus provides one of the deepest ERO sample ever reported. It is noted that we obtained mostly the same results using other model parameters used in Wu et al. (1998) and Williams et al. (1999).

For a comparison, we overplotted the result of G.P. Smith et al. (2002) and Wehner et al. (2002) without the sample of A 2390 in figure 9. Both ERO samples were made by targeting lensing cluster fields, and selected by the same color criterion as ours ($R_c - K' > 5.3$). We also overplotted the results by blank-field ERO searches performed by Daddi et al. (2000), Roche et al. (2002), and Moustakas et al. (1997). G.P. Smith et al. (2002) surveyed lensed EROs behind 10 massive clusters of galaxies around $z \sim 0.2$ to a depth of $K \sim 20.6$, and measured the surface density of $1.2\,\mathrm{arcmin}^{-2}$ for $R_c - K \geq 5.3$. They corrected the amplification effect from gravitational lensing using their own lens model, and estimated the corrected surface densities at $K \leq 21.6$ as $2.5\,\mathrm{arcmin}^{-2}$. The values are very similar to our result. As shown in figure 9, there is little difference between both samples at the overlapping magnitude ranges, and can be considered to be within error bars for $R_c - K' \geq 5.3$ samples.

For a surface-density enhancement evaluation, we also calculated corrected surface densities in the areas which are shown in figure 3 by rectangles with dotted lines. In MS 0451.6−0305 field, 6 EROs in $\sim 0.6\,\mathrm{arcmin}^2$ area, and the corrected surface density is $46.2\,\mathrm{arcmin}^{-2}$ down to $K'_{source} = 21.0$ at $z_{source} = 3.0$, or 30.8 at $z_{source} = 1.5$. In MS 0440.5+0204 field, 3 EROs brighter than $K' = 20.6$ are within $0.1\,\mathrm{arcmin}^2$ area, and corrected surface density is $62.5\,\mathrm{arcmin}^{-2}$ down to $K'_{source} = 21.0$ at $z_{source} = 1.5$. They are more than 7-times than the average values reported by previous surveys. It is the same trend with the sample of G.P. Smith et al. (2002),

which indicates that the numbers and sky distributions of EROs are very different in each field of view. Those are also consistent with the results by other wide field ERO surveys, which suggest the clustering properties of EROs (Daddi et al. 2001; Thompson et al. 1999). The most different property of our sample from G.P. Smith et al. (2002)'s is that most EROs identified in MS 0451.6−0305 show the colors which are common in dusty star-forming galaxies at high redshift (figure 7), which indicate their strong star-formation activities, while most EROs are passively evolved objects in Smith et al.'s. Daddi et al. (2002) suggested that the strength of clustering is stronger in the old ERO population than that of dusty starburst EROs, and our results on the MS 0451.6−0305 may be a very rare case. It may indicate that the deeper is the depth of observation, for example down to $K' = 20.5$, the more will the ratio of dusty starbursts in ERO population increase. This is suggested by Smail et al. (2002b) with a radio-selected ERO sample, and the ratio of the dusty population to the passive one is comparable at brighter magnitudes (Cimatti et al. 2002). However, we also have to pay attention to the effect of the selection bias in our sample, which is made by targeting to lensed SCUBA sources, because it may increase the possibility of detecting dusty EROs.

In the deepest magnitude ranges of our sample, there are deficiencies of EROs compared to Wehner et al. (2002), while the uncertainties of ours and of their results are very large. This is because both surveys have a very limited region coverages and also suffer from field variances of ERO numbers.

4.3. *Lensed Dusty Star-Forming Galaxies around SMM J04542−0301?*

4.3.1. *Possible giant extremely red arc*

As mentioned in the previous section, 7 EROs are concentrated within a 0.6 arcmin^2 sky area, and its corrected surface density is more than 7-times the average value (figure 9). For confirming the over density, however we have to take care of the fact that there are EROs which are possible to be gravitationally lensed and separated (splitted) into several images (e.g. "A1" to "A4" in figure 4). These sources are well aligned in parallel to the "Blue Arc", which is believed to be gravitationally elongated and split. If they are constructing an extremely red arc, the surface density will be decreased to 7.7 arcmin^{-2} for $z_{\rm source} = 1.5$ or 23.1 arcmin^{-2} for $z_{\rm source} = 3.0$ at $K'_{\rm source} < 21.0$; however it is still a density enhancement.

For discussing the possibility of this lensing effect, we used the elliptical lens model, which was applied to a surface number count. The lens model also gives us a possibility to estimate the redshifts of lensed objects without any spectroscopic data, and may be able to set constraints on the spatial distribution of some EROs. We compared the critical curves on the image plane for different source plane redshifts, as shown in figure 10. We also overplotted the contour map of soft X-ray (0.2–1.5 keV) image of Chandra observation[4] with 15000 s exposure[5] to show the adequacy of our lensing model for approximating the cluster mass distribution. The

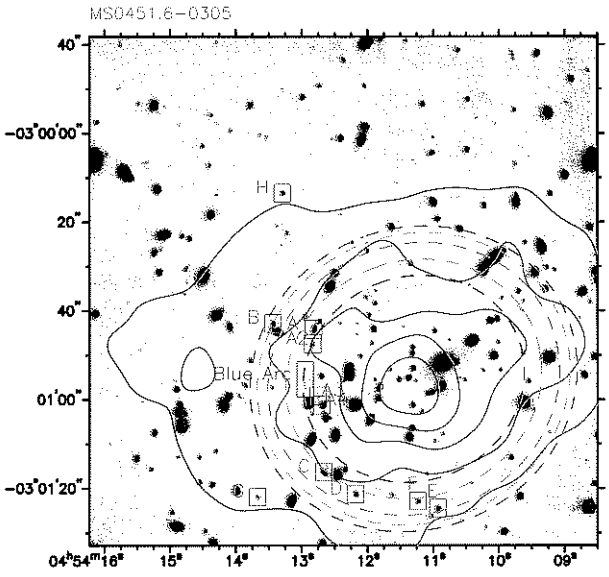

Fig. 10. K' image of MS 0451.6−0305 with the contour of soft (0.2–1.5 keV) X-ray image taken by Chandra with a 10 ks exposure overplotted. The levels show between 1.0×10^{-8} to 5.0×10^{-8} photons cm^{-2} s^{-1} pix^{-1} with the same interval. The critical curves for the source at $z_{\rm source} = 1.2$, 1.5, 2.0, 2.5, and 3.0 are also shown as dotted blue, light blue, green, orange, and red lines, respectively. The objects denoted in figure 4 are all shown encircled by squares (red rectangles represent EROs).

images were retrieved from the Chandra archive, and we used CIAO software for extracting the soft band photon, combining each exposure and smoothing the resultant image. We applied 5-pixel Gaussian adaptive smoothing for the image using the csmooth task. The shapes of the inner X-ray contours and the used mass distribution are in good agreement for a first-order approximation of the mass distribution.

The sources "A1" to "A4" are very near to the critical curve, especially for $z_{\rm source} = 1.2$ in figure 10. Therefore, it is possible that they are forming a large extremely red arc, and are split images of an object at $z \sim 1.2$. If they are, their colors must be very similar to each other, assuming no extinction differences along each light path. The colors of "A1" and "A4" are different, although the optical band magnitudes may be contaminated by other sources which are near to these objects. There remains a possibility that the colors of "A2" and/or "A3" will coincide with those of "A1" and/or "A4" because "A2" and "A3" are detected only in the K' band, and a color comparison was unavailable. Although the estimated redshifts is $z = 1.2$ by our lensing model, this is inconsistent with a photometric redshift of $z > 2.3$ derived from the radio vs sub-mm index if they are counterparts of the sub-mm source. However it is possible that the photometric redshift estimate is not appropriate if the assumed dust temperature for the SED model is not correct (Blain et al. 2003). In fact, it is suggested that there is a diversity of the dust temperature of sub-mm sources based

[4] Based in part on data retrieved from the Chandra Data Archive (CDA), a part of the Chandra X-ray Observatory Science Center (CXC) which is operated for NASA by the Smithsonian Astrophysical Observatory.

[5] Because of spurious counts on a soft band image, we did not use the deeper (45000 s exposure) ACIS-S image for our analysis. For hard band image analysis, we used it.

on a sample of sub-mm sources with redshifts (Chapman et al. 2003).

It should also be noted that X-ray emission can not be completely fitted by a simple elliptical mass distribution. It is elongated to north-west direction, which has already been suggested by Donahue and Stocke (1995) using the ROSAT image, and the X-ray contours are uneven (figure 10). For a more detailed discussion concerning the reality of a giant extremely red arc, it is necessary to use a lens model which is more sensitive to the local mass distribution, like that by Kneib et al. (1996). It will be considered in a future coming paper with some redshifts of bright objects and blue arcs.

4.3.2. SED fitting for a redshift estimation

For investigating the spatial clustering properties of these EROs and red galaxies near SMM J04542−0301, we used a SED fitting for deriving the photometric redshifts for 6 objects among those (extremely) red objects ("A4", "B", "C", "D", "E", and "F"), which had confirmed magnitudes in several bands. Because the optical bands' lights of "A1" may be coming from a physically different source (optical centroids are more than $1''$ apart from K' image's centroid), we eliminated "A1" from a list of our SED fitting. To avoid the effect of contamination from other surrounding sources, we used $1''$ diameter magnitudes for sources "A4", "B", and "C", while they were $2''$ for others. We used hyperz for the calculation, by stepping the extinction from $A_V = 0.0$ to 5.0 using the extinction formula by Calzetti et al. (2000), and sought the best solution in the range of $0.0 \leq z \leq 10.0$. As shown in figure 11, many objects, except for "D" and "F", were fitted by SEDs of galaxies at high redshift ($z \geq 2.6$), which are consistent with the photometric redshift from sub-mm to radio index ($z_{\rm photo} \geq 2.3$), although with relatively small extinction [$E(B-V) \sim 0.15$–0.30]. These extinction values are equal to, or slightly higher than, the median of those of Lyman break galaxies at $z \sim 3$ (Steidel et al. 1999; Shapley et al. 2001). Their $R - K'$ colors are more than 5.0, and thus redder than the sub-mm source Lyman break galaxy "W-MMD11" (Chapman et al. 2002c). They also have red $J - K'$ colors (> 2.3), and their properties are similar to those of a red massive galaxy population at high redshift ($2 < z < 4$), revealed by the Faint InfraRed Extragalactic Survey (FIRES; Franx et al. 2003; van Dokkum et al. 2003). This red color can only be explained by a composite of the stellar ages with ≥ 300 Myr and a certain amount of obscuration by dust (Franx et al. 2003). The ages for our red sources best fitted by our analysis range from 0.5 to 1.2 Gyr. Daddi et al. (2003) suggested that their strong clustering at $2 < z < 4$ and our result can show the property. The derived extinction for "D" is large (0.89), and it is a plausible nearby candidate of a sub-mm source. Since the magnitudes of "A4" may be contaminated by neighboring foreground objects and/or contribution from diffuse emission by the cluster, the fluxes in the optical bands may be mainly coming from other sources. Therefore, it can have redder colors than those listed in table 1, and we could not eliminate the possibility of "A4" as being a counterpart of a sub-mm source. If so, its redshift can be higher, and may be the same as those of "B" and "C". If "A1" to "A4" are constructing an extremely red arc, it is another plausible candidate of a sub-mm source, and they may have a spatial concentration with "B" and "C".

It is noted that the results of photometric redshifts using different extinction models, like Fitzpatrick (1986) for Magellanic Large Cloud or Prévot et al. (1984) and Bouchet et al. (1985) for the Small Megellanic Cloud, provided slightly higher redshifts.

By combining the result of our analysis, we can suggest one possibility that this extended sub-mm flux is coming from a high redshift object, which must be lensed by a foreground cluster, and there may be a contribution from a lower redshifted ($z \sim 0.5$) dusty object, "D". Since there is some evidence that Lyman break galaxies are not main contributor to the cosmic sub-mm background radiation (Adelberger, Steidel 1999; Webb et al. 2002), "B", "C", and "E" may be eliminated from the counterpart candidates; however, they may be spatially clustering near to the sub-mm emission. For secure counterpart identification and confirming the speculation of their clustering properties, it is essential to perform a deep radio interferometric observation and spectroscopic follow-up observations in optical or near-infrared wavelengths.

Using Chandra hard (4–8 keV) X-ray images, which was produced from the same data as that for figure 10, we checked the coincidences of X-ray detections around sub-mm sources in the MS 0451.6−0305 region, although no counterparts were identified. This is consistent with the result of previous studies because about 50000-s exposure by Chandra is not sufficient for detecting the X-ray flux from a large amount of sub-mm sources (Alexander et al. 2003; Waskett et al. 2003).

5. Summary

We performed deep near-infrared and optical imaging of two massive clusters of galaxy fields. By combining this data with photometric information taken from the deep WFPC2/F702W image, we identified EROs in each field, 8 in MS 0451.6−0305 and 5 in MS 0440.5+0204 with $R_{\rm c} - K' \geq 5.3$, and $K' < 22.0$, in a $2' \times 2'$ field of view. Our sample provides one of the deepest sample of EROs ever reported. The surface density of our whole-area sample shows good agreement with other previous samples at the bright part. At the faint end, the number of EROs is slightly deficient compared to the previous work, though it is within the error bars.

We identified 7 EROs ($R_{\rm c} - K' \geq 5.3$) and 3 red objects ($I_{\rm c} - K' > 4.0$) with $K' \leq 20.6$ within 0.6 arcmin^2 of an extended SCUBA source in the MS 0451.6−0305 field. Our investigation using a lens model provided a value of surface density of EROs of $\sim 46\,{\rm arcmin}^{-2}$ for $K'_{\rm source} < 21.0$, showing a surface-density enhancement of extremely red galaxies, even after a correction of the lensing effect. It is possible that 4 sources, named "A1" to "A4", constitute an extremely red-giant arc, and that the best-fit redshift by our model is $z \sim 1.2$. The photometric redshift for a sub-mm source, derived based on the sub-mm to radio index, does not give consistent redshift. We also investigated the optical and near-infrared photometric features for the 6 red sources, and identified that 4 of them have SEDs which are typical of high-redshift objects. Their extinctions are typical, or slightly higher, values compared to those of Lyman break galaxies at $z \sim 3$. Our redshift estimation

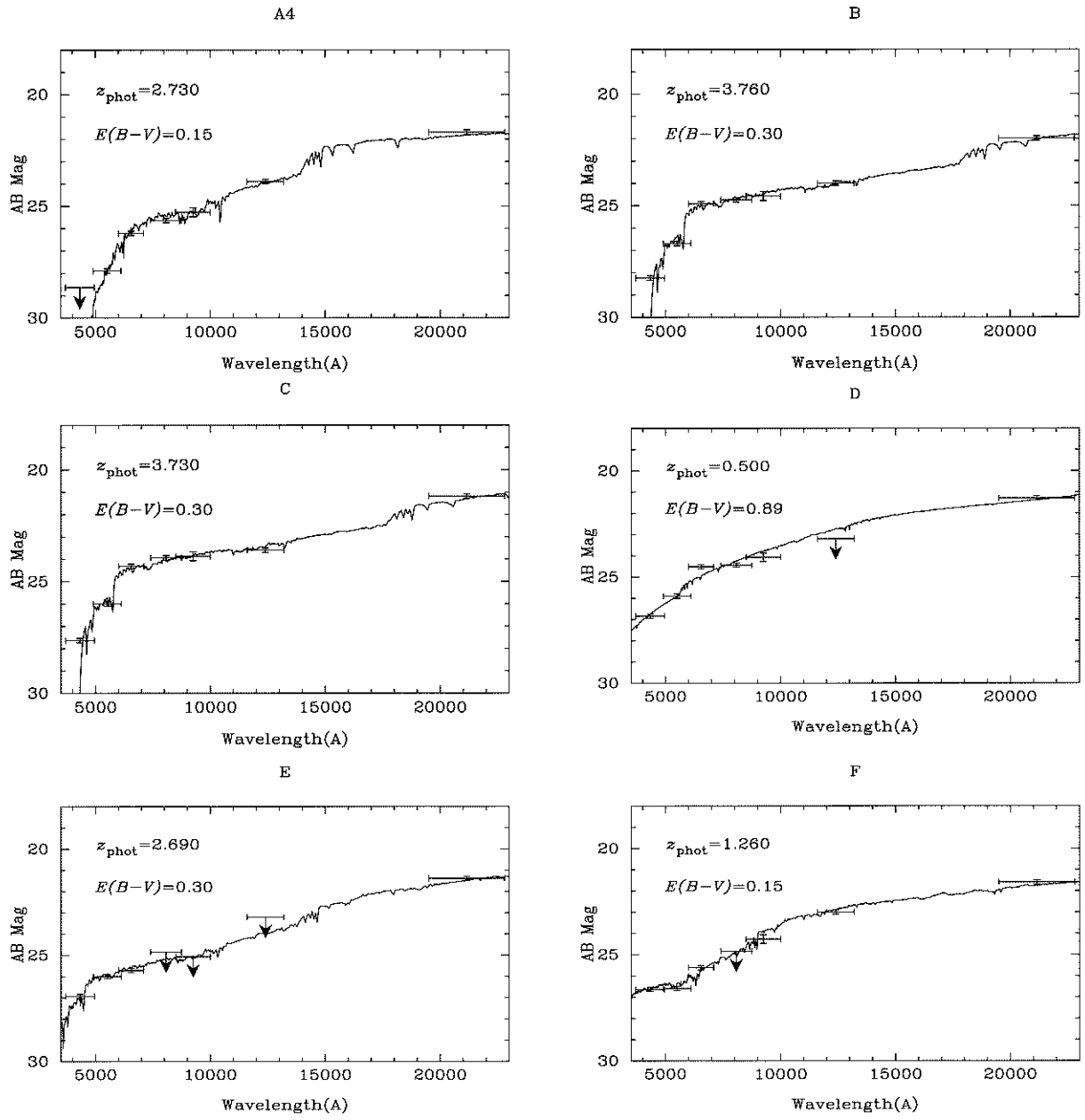

Fig. 11. Fitted SEDs for six (extremely) red objects around SMM J04542−0301.

for "A4" based on an SED fitting is consistent with that from sub-mm to radio index, and it is possible to consider that "A1" to "A4" are lensed extremely red sources at $z > 2.5$, and a counterpart of an extended sub-mm source. One source with severe extinction is identified at a lower redshift ($z \sim 0.5$), and is one of the candidates of contributors to the extended sub-mm flux. For revealing their clustering properties and the relation with extended sub-mm emission, a spectroscopic follow-up observation in the optical and/or near-infrared wavelength is essential.

This study is based mainly on data collected at Subaru Telescope, and those obtained from the data archive at the Astronomical Data Analysis Center, which is operated by the National Astronomical Observatory. The authors thank an anonymous referee for valuable comments and suggestions for improving the manuscript. We are grateful to all Subaru staff members for their enormous help during our observations. T.T. thanks to Dr. Kentaro Motohara and Dr. Chris Simpson for their enormous help during the observation and data reduction, Dr. Yoshitomo Maeda for giving instructions on the CIAO software for reducing the Chandra image. T.T. also thanks the staff of the archive system of the Space Telescope Science Institute for their help in retrieving the HST data. This work is partly supported by the Ministry of Education, Culture, Sports, Science and Technology under Grant No. 12740126. K.N. has been financially supported by a JSPS Fellowship.

References

Adelberger, K. L., & Steidel, C. C. 2000, ApJ, 544, 218
Alexander, D. M., et al. 2003, AJ, 125, 383
Baba, H., et al. 2002, Rep. Natl. Astron. Obs. Japan, 6, 23 (in Japanese)
Barger, A. J., Cowie, L. L., & Richards, E. A. 2000, AJ, 119, 2092
Barger, A. J., Cowie, L. L., Sanders, D. B., Fulton, E., Taniguchi, Y., Sato, Y., Kawara, K., & Okuda, H. 1998, Nature, 394, 248
Bertin, E., & Arnouts, S. 1996, A&AS, 117, 393
Blain, A. W., Barnard, V. E., & Chapman, S. C. 2003, MNRAS, 338, 733
Blain, A. W., Smail, I., Ivison, R. J., Kneib, J.-P., & Frayer, D. T. 2002, Phy. Rep., 369, 111
Bolzonella, M, Miralles, J-M, & Pelló, R. 2000, A&A, 363, 476
Bouchet, P., Lequeux, J., Maurice, E., Prévot, L., & Prévot-Burnichon, M. L. 1985, A&A, 149, 330
Bruzual, G. A., & Charlot, S. 1993, ApJ, 405, 538
Calzetti, D., Armus, L., Bohlin, R. C., Kinney, A. L., Koornneef, J., & Storchi-Bergmann, T. 2000, ApJ, 533, 682
Casali, M., & Hawarden, T. 1992, UKIRT Newsletter, 4, 33
Chapman, S. C., Blain, A. W., Ivison, R. J., & Smail, I. R. 2003, Nature, 422, 695
Chapman, S. C., Scott, D., Borys, S., & Fahlman, G. G. 2002a, MNRAS, 330, 92
Chapman, S. C., Shapley, A., Steidel, C., & Windhorst, R. 2002c, ApJ, 572, L1
Chapman, S. C., Smail, I., Ivison, R. J., & Blain, A. W. 2002b, MNRAS, 335, 17
Cimatti, A., et al. 2002, A&A, 381, L68
Cimatti, A., Andreani, P., Röttgering, H., & Tilanus, R. 1998, Nature, 392, 895
Daddi, E., et al. 2002, A&A, 384, L1
Daddi, E., et al. 2003, ApJ, 588, 50
Daddi, E., Broadhurst, T., Zamorani, G., Cimatti, A., Röttgering, H., & Renzini, A. 2001, A&A, 376, 825
Daddi, E., Cimatti, A., Pozzetti, L., Hoekstra, H., Röttgering, H. J. A., Renzini, A., Zamorani, G., & Mannucci, F. 2000, A&A, 361, 535
Donahue, M., & Stocke, J. T. 1995, ApJ, 449, 554
Eales, S., et al. 1999, ApJ, 515, 518
Ellingson, E., Yee, H. K. C., Abraham, R. G., Morris, S. L., & Carlberg, R. G. 1998, ApJS, 116, 247
Fitzpatrick, E. L. 1986, AJ, 92, 1068
Fox, M. J., et al. 2002, MNRAS, 331, 839
Franx, M., et al. 2003, ApJ, 587, L79
Franx, M., Illingworth, G. D., Kelson, D. D., van Dokkum, P. G., & Tran, K.-V. 1997, ApJ, 486, L75
Frayer, D. T., Armus, L., Scoville, N. Z., Blain, A. W., Reddy, N. A., Ivison, R. J., & Smail, I. 2003, AJ in press (astro-ph/0304043)
Frayer, D. T., Smail, I., Ivison, R. J., & Scoville, N. Z. 2000, AJ, 120, 1668
Fruchter, A. S., & Hook, R. N. 2002, PASP, 114, 144
Fukugita, M., Ichikawa, T., Gunn, J. E., Doi, M., Shimasaku, K., & Schneider, D. P. 1996, AJ, 111, 1748
Gioia, I. M., Maccacaro, T., Schild, R. E., Wolter, A., Stocke, J. T., Morris, S. L., & Henry, J. P. 1990, ApJS, 72, 567
Gioia, I. M., Shaya, E. J., Le Fèrve, O., Falco, E. E., Luppino, G. A., Hammer, F. 1998, ApJ, 497, 573
Holland, W. S., et al. 1999, MNRAS, 303, 659
Holtzman, J. A., Burrows, C. J., Casertano, S., Hester, J. J., Trauger, J. T., Watson, A. M., & Worthey, G. 1995, PASP, 107, 1065
Hughes, D. H., et al. 1998, Nature, 394, 241
Ivison, R. J., et al. 2002, MNRAS, 337, 1
Ivison, R. J., Smail, I., Barger, A. J., Kneib, J.-P., Blain, A. W., Owen, F. N., Kerr, T. H., & Cowie, L. L. 2000, MNRAS, 315, 209
Ivison, R. J., Smail, I., Frayer, D. T., Kneib, J.-P., & Blain, A. W. 2001, ApJ, 561, L45
Kashikawa, N., et al. 2002, PASJ, 54, 819
Kneib, J.-P., Ellis, R. S., Smail, I., Couch, W. J., & Sharples, R. M. 1996, ApJ, 471, 643
Kormann, R., Schneider, P., & Bartelmann, M. 1994, A&A, 284, 285
Landolt, A. U. 1992, AJ, 104, 340
Ledlow, M. J., Smail, I., Owen, F. N., Keel, W. C., Ivison, R. J., & Morrison, G. E. 2002, ApJ, 577, L79
Lilly, S. J., Eales, S. A., Gear, W. K. P., Hammer, F., Le Fèvre, O., Crampton, D., Bond, J. R., & Dunne, L. 1999, ApJ, 518, L641
Lutz, D., et al. 2001, A&A, 378, 70
Miyazaki, S., et al. 2002, PASJ, 54, 833
Motohara, K., et al. 2002, PASJ, 54, 315
Moustakas, L. A., Davis, M., Graham, J. R., Silk, J., Peterson, B. A., & Yoshii, Y. 1997, ApJ, 475, 445
Pettini, M., Steidel, C. C., Adelberger, K. L., Dickinson, M., & Giavalisco, M. 2000, ApJ, 528, 96
Pozzetti, L., & Mannucci, F. 2000, MNRAS, 317, L17
Prévot, M. L., Lequeux, J., Prévot, L., Maurice, E., & Rocca-Volmerange, B. 1984, A&A, 132, 389
Roche, N. D., Almaini, O., Dunlop, J., Ivison, R. J., & Willott, C. J. 2002, MNRAS, 337, 1282
Schneider, P., Ehlers, J., & Falco, E. E. 1992, Gravitational Lenses (Berlin: Springer), 266
Scott, S. E., et al. 2002, MNRAS, 331, 817
Shapley, A., Steidel, C. C., Adelberger, K. L., Dickinson, M., Giavalisco, M., & Pettini, M. 2001, ApJ, 562, 95
Smail, I., Ivison, R. J., & Blain, A. W. 1997, ApJ, 490, L5
Smail, I., Ivison, R. J., Blain, A. W., & Kneib, J.-P. 1998, ApJ, 507, L21
Smail, I., Ivison, R. J., Blain, A. W., & Kneib, J.-P. 2002a, MNRAS, 331, 495
Smail, I., Ivison, R. J., Kneib, J.-P., Cowie, L. L., Blain, A. W., Barger, A. J., Owen, F. N., & Morrison, G. 1999, MNRAS, 308, 1061
Smail, I., Owen, F. N., Morrison, G. E., Keel, W. C., Ivison, R. J., & Ledlow, M. J. 2002b, ApJ, 581, 844
Smith, G. P., et al. 2002, MNRAS, 330, 1
Smith, G. P., Treu, T., Ellis, R. S., & Smail, I. 2001, ApJ, 562, 635
Smith, J. A., et al. 2002, AJ, 123, 2121
Stanford, S. A., Eisenhardt, P. R., & Dickinson, M. 1998, ApJ, 492, 461
Stanford, S. A., Eisenhardt, P. R., Dickinson, M., Holden, B. P., & De Propis, R. 2002, ApJS, 142, 153
Steidel, C. C., Adelberger, K. L., Giavalisco, M., Dickinson, M., & Pettini, M. 1999, ApJ, 519, 1
Thompson, D., et al. 1999, ApJ, 523, 100
van Dokkum, P. G., et al. 2003, ApJ, 587, L83
Waskett, T. J., et al. 2003, MNRAS, 341, 1217
Webb, T. M., et al. 2003, ApJ, 582, 6
Wehner, E. H., Barger, A. J., & Kneib, J.-P. 2002, ApJ, 577, L83
Williams, L. L. R., Navarro, J. F., & Bartelmann, M. 1999, ApJ, 527, 535
Wu, X. P., Chiueh, T., Fang, L.-Z., & Xue, Y.-J. 1998, MNRAS, 301, 861
Yagi, M., Kashikawa, N., Sekiguchi, M., Doi, M., Yasuda, N., Shimasaku, K., & Okamura, S. 2002, AJ, 123, 66
Yun, M. S., & Carilli, C. L. 2002, ApJ, 568, 88

PASJ: Publ. Astron. Soc. Japan **55**, 871–877, 2003 August 25

Acceleration Method of Neighbor Search with GRAPE and Morton Ordering

Takayuki R. SAITOH
Division of Physics, Graduate School of Science, Hokkaido University, N10W8, Sapporo 060-0810
takayuki@astro1.sci.hokudai.ac.jp
and
Jin KODA*
National Astronomical Observatory, 2-21-1 Osawa, Mitaka, Tokyo 181-8588
jin.koda@nao.ac.jp

(Received 2003 April 14; accepted 2003 May 20)

Abstract

We describe a new method to accelerate neighbor searches on GRAPE, i.e. a special-purpose hardware that efficiently calculates the gravitational forces and potentials in N-body simulations. In addition to gravitational calculations, GRAPE simultaneously constructs lists of neighbor particles that are necessary for Smoothed Particle Hydrodynamics (SPH). However, the data transfer of the neighbor lists from GRAPE to the host computer is time-consuming, and can be a bottleneck. In fact, the data transfer can take about the same time as the calculations of the force themselves. Making use of GRAPE's special treatment of neighbor lists, we can reduce the amount of data transfer if we search neighbors in the order that the neighbor lists, constructed in a single GRAPE run, overlap each other. We find that the Morton ordering requires very low additional calculation and programming costs, and results in successful speed-up on data transfer. We show some benchmark results in the case of GRAPE-5. Typical reduction in transferred data becomes as much as 90%. This method is suitable not only for GRAPE-5, but also for GRAPE-3 and the other versions of GRAPE.

Key words: cosmology: large-scale structure of universe — galaxies: formation — galaxies: ISM — methods: numerical

1. Introduction

GRAPE (GRAvity PipE; Sugimoto et al. 1990) is a special-purpose hardware that calculates Newtonian gravitational forces efficiently in large-scale N-body simulations. A series of GRAPE versions was developed by Ito et al. (1990; GRAPE-1), Ito et al. (1991; GRAPE-2), Okumura et al. (1993; GRAPE-3), Makino et al. (1997; GRAPE-4), and Kawai et al. (2000; GRAPE-5). GRAPE is connected with, and controlled by, a typical workstation or PC. The host computer requests GRAPE to calculate gravitational forces. Force integration and particle pushing are all done on the host computer. Owing to its high performance, GRAPE has been a powerful tool for solving astronomical N-body problems, such as those related to star cluster evolution (Makino 1996), black hole spiral-in (Makino, Ebisuzaki 1996), formation of planets (Kokubo, Ida 1998), and formation of central cusps in dark matter halos (Fukushige, Makino 1997).

In addition to efficient gravitational calculations, GRAPE performs parallel gathering of neighbor particles, and returns neighbor lists to the host computer if requested. Since searching neighbors is one of the most time-consuming routines in some particle simulations with close interactions, such as the Smoothed Particle Hydrodynamics (SPH), the neighbor lists from GRAPE are advantageous in speeding up those simulations. Thus, SPH is often combined with N-body calculations using GRAPE. Pioneering work on the GRAPE-SPH method was done by Umemura et al. (1993), using GRAPE-1A. Steinmetz (1996) reported the high performance of the GRAPE-SPH method using GRAPE-3. The GRAPE-SPH method has been successfully applied to a number of topics, e.g., fragmentation of molecular clouds (Klessen 1997), and galaxy formation (Steinmetz, Müller 1995; Weil et al. 1998; Mori et al. 1999; Koda et al. 2000a,b).

Despite the high performance of GRAPE-SPH, searching neighbors is still a massive routine in full calculations (Steinmetz 1996). In particular, the data transfer of neighbor lists between GRAPE and the host computer is a bottleneck for speed-up. Steinmetz (1996) pointed out that, owing to the specification of GRAPE, the amount of the data transfer can be reduced if the neighbor lists for particles, returned from GRAPE at once, overlap each other (see section 2 for details); in the case of GRAPE-3 that can construct 8 neighbor lists for 8 particles simultaneously, if the lists are completely the same, the communication time for the 8 lists becomes as fast as that for a single list. In order to make the lists overlap at least partially, Steinmetz (1996) sorted the particles into the X-coordinate order before the GRAPE call, because the particles, having similar neighbor lists, must have similar positions, and thus similar X-coordinates. This approach reduced the time consumed in entire neighbor searches by 10–20%, in simulations using a few tens of thousands of particles and GRAPE-3.

This approach, however, becomes less effective when the number of particles increases, because the particles with similar X-coordinates are more likely to have very different

* JSPS Research Fellow.

Y-, Z-coordinates. In this paper, we introduce another ordering method, i.e. the Morton-ordering method, for GRAPE neighbor searches, which keeps track of original 3-dimensional particle coordinates, and are independent of the number of particles. We show some test calculations of neighbor searches using GRAPE-5 and Morton ordering. The Morton-ordering method has been suggested for some parallel tree algorithms for N-body simulations (Barnes, Hut 1989; Warren, Salmon 1995), and is now being applied to searching neighbors in GRAPE-SPH.

We briefly review some GRAPE hardware specifications related to searching neighbors in section 2, and Morton ordering in section 3. Test calculations and results are shown in sections 4 and 5, respectively. A summary appears in section 6.

2. GRAPE: Specification for Neighbor Search

A GRAPE series is a special-purpose board, similar to a graphic board, used to accelerate gravitational-force calculations in N-body problems. It is connected with, and controlled by, a host computer, i.e. a typical workstation or PC. The host computer sends particle positions and masses to GRAPE, and GRAPE calculates the gravitational forces and potentials, sending them back to the host computer. GRAPE can also return neighbor particle lists and, thus, is suitable for simulations with close interactions, such as SPH simulations. The data transfer of the neighbor lists, however, takes much more time than that for the others, i.e. for a single particle, typically sixty words for a neighbor list should be transferred, while only ten words are transferred for mass, position, force, potential, gravitational softening, and radius of the particle. We will introduce a method to speed up this data transfer in section 3. Though we describe the case for the fifth version of the GRAPE series (GRAPE-5), the method is also well suited for GRAPE-3 and the other versions of GRAPE. Detailed designs of the GRAPE-5 hardware are described in Kawai et al. (2000). Hence, we give a brief review, and necessary details for our new neighbor-searching method.

The main engine of a GRAPE-5 board is composed of G5 chips. The G5 chip is a custom LSI chip, which calculates gravitational forces and potentials. One GRAPE-5 board has eight G5 chips, each of which calculates the forces on 12 particles simultaneously; hence, one board calculates the forces on $8 \times 12 = 96$ particles at once. The gravitational force $\boldsymbol{f}_i$ on a particle i is derived by first calculating the force $\boldsymbol{f}_{ij}$ between two particles (i and j), and then summing them up among all particles $\sum_j \boldsymbol{f}_{ij}$. The G5 chip can also check whether a particle j is a neighbor of a particle i, by comparing the square of the distance r_{ij}^2 between i and j, with the square of the radius h_i of i, as $r_{ij}^2 < h_i^2$.

The neighbor lists, output from the G5 chips, are stored in special memories on the GRAPE-5 board. There are two memory units on a single GRAPE-5 board, each of which stores the neighbor lists from four of the eight G5 chips on a board, and thus, for $4 \times 12 = 48$ particles. GRAPE-5 does not keep the neighbor lists in a simple lengthy manner, such that all neighbors of the 48 particles occupy individual memory space, but in a way that keeps the lists as particle indices and flags. For example, when one particle has a neighbor list of (8, 11, 22, 41, 49) and another has (3, 7, 11, 23, 41), these two lists are kept as a convolved particle index list (3, 7, 8, 11, 22, 23, 41, 49) and binary flags (01, 01, 10, 11, 10, 01, 11, 10). The host computer receives these indices and flags from GRAPE, and deconvolves these into individual neighbor lists for the two particles. One neighbor memory unit, of the two on a GRAPE-5 board, stores the neighbor lists for the 48 particles. Thus, the above convolved list and binary flags are made for the 48 particles.

This particular operation for the neighbor lists provides room to speed up the data transfer and, hence, the neighbor search. Considering the case that each particle has $n_s = 60$ neighbor particles, if the 48 particles have completely different neighbors, the data transferred from GRAPE-5 to the host computer are $48 \times 60 = 2880$ words for the convolved list, and 2880 words for the binary flags. On the other hand, if we can arrange the 48 particles so that they have perfectly identical neighbor lists, the amount of data is significantly reduced to 60 words for the convolved list and 60 words for the binary flags, which means that the communication time is reduced by $1/48$.[1] Hence, we can reduce the communication time for searching neighbors with GRAPE, by arranging the 48 particles so that their neighbors overlap significantly.

3. GRAPE Neighbor Search with Morton Ordering

A GRAPE-5 board searches neighbors for 96 particles simultaneously in a single GRAPE run. In large N-body simulations, the GRAPE run is repeated $N/96$ times. Each of the two memory units on a GRAPE-5 board keep the neighbor lists for $96/2 = 48$ particles in a single run, and the lists are transferred from GRAPE to the host computer. According to the GRAPE specifications in section 2, we can reduce the amount of the transferred data if we choose the 48 particles, for a single memory in a single run, so that their neighbors overlap each other. The cost of the data transfer is reduced by increasing the fraction of the overlap.

In order to make the neighbor lists overlap, we should choose 48 intrinsically neighboring particles, i.e. particles with similar coordinates, for a single GRAPE run. Based on this idea, Steinmetz (1996) sorted all the particles according to their X-coordinates, and succeeded in reducing the communication cost between GRAPE-3 and a host computer. This method expects that the particles arranged by X-coordinates would more frequently have similar (X, Y, Z)-coordinates than randomly distributed particles. However, this method becomes less effective in very large GRAPE-SPH simulations, because the radius h for searching neighbors becomes smaller in larger simulations, and thus, two particles with similar X-coordinates would more frequently have quite different Y-, Z-coordinates, which makes the separation of the two more than h. Therefore, we suggest the use of Morton ordering, rather than X-coordinate ordering. Morton ordering naturally translates the (X, Y, Z)-coordinates into a 1-D space, with sufficiently maintaining the original 3-D structure. Morton ordering

[1] In actual operations, a particle index and binary flag, for a neighbor particle, are not separately treated. GRAPE stores them in a single 64-bits memory block; the higher 48-bits for the flag, and the lower 16-bits for the index (see Kawai et al. 2000 for details).

has been suggested for a parallel tree code for gravitational calculations (Barnes, Hut 1989).

In the Morton ordering, the 3-D coordinates $(X, Y, Z) = (0.x_1x_2x_3\ldots, 0.y_1y_2y_3\ldots, 0.z_1z_2z_3\ldots)$ of a particle are translated into a 1-D *key* as $0.x_1y_1z_1x_2y_2z_2\ldots$. Then, the particles are sorted according to those keys. Since those 1-D keys sufficiently have the memory of the original 3-D coordinates, two particles with similar keys lie close to each other in the 3-D space as well. In actual operations, the key is constructed in a binary space and, hence, can be simply produced by bit-shift and add. Thus, the costs for the key construction in calculations and the coding by a programmer are quite low. Additional time for sorting is also negligible. A demonstration of the Morton ordering in a 2-D case for 3000 particles is shown in figure 1. The particles are randomly and uniformly distributed in a unit circle, and connected in the Morton order (key order) with the single stroke of a pen. It is evident that the Morton ordering arranges the particles in such a way that those with similar 2-D coordinates lie close to each other in the key space (1-D), and that the particles with similar keys must have quite similar neighbor lists. Hence, the Morton ordering is effective to make the neighbor lists of the 48 particles overlap.

4. Test Calculations

We test the efficiency of the above new method (GRAPE+Morton ordering), in comparison with two other methods using GRAPE. We distribute particles in space, search neighbors for those particles using GRAPE, and measure the time consumed for the neighbor search. Before starting the GRAPE neighbor search, we rearrange the particles (1) in a *random* order (hereafter, R-ordering), i.e. with no rearrangement, (2) in a X-coordinate order (X-ordering), and (3) in a Morton order (M-ordering). The last two orderings will actively make the 48 neighbor lists, stored on a single GRAPE memory unit, overlap each other, which improves the efficiency of the GRAPE neighbor search, as discussed in section 3.

In actual calculations, such as cosmological and galaxy formation simulations, there appear various density distributions. Matter is uniformly distributed in the early stage of the Universe, gradually assembled and collapsed by gravity, and then forms nearly isothermal objects. Hence, we adopt spherically symmetric density profiles, $\rho(r) \propto r^n$, with the index n of 0.0 (uniform) and -2.0 (isothermal), for test calculations. The density profiles are constructed by randomly and uniformly distributing particles in a unit sphere, and stretching the distribution by means of a radial coordinate transformation, i.e. $r_{\rm new} = r_{\rm old}^{3/(3+n)}$. We also test the Hernquist profile (Hernquist 1990) as a realistic density model of dark matter halo, i.e.

$$\rho(r) = \frac{1}{2\pi}\frac{a}{r}\frac{1}{(r+a)^3}, \tag{1}$$

where the core and truncation radii are set to $a = 0.1$ and $r_{\rm max} = 1.0$, respectively. The number of particles, in the test calculations, is changed from 10000 to 100000 with a step of 10000, which may be possible numbers for actual SPH simulations with the direct $O(N^2)$ calculations of GRAPE-5. The neighbor search radius h of each particle is set at the distance of its n_sth nearest particle, and we set $n_s = 60$ when no descriptions are given explicitly. This definition of h is often used in SPH calculations. We repeat the neighbor search 10 times for each test calculation, and average them to get benchmark results, since the results are slightly swayed in individual runs.

For the test calculations, we use a single GRAPE-5 board connected with an Alpha 264 processor computer with a clock frequency of 833 MHz, which is one of the GRAPE systems in the Mitaka Under Vineyard (MUV), run underground at the National Astronomical Observatory of Japan.

5. Results

5.1. *Consumption Time*

Table 1 summarizes the consumption times in neighbor searches with GRAPE, in cases using random ordering (R-ordering), X-coordinate ordering (X-ordering), and Morton ordering (M-ordering). The tabulated times include both the data transfers between GRAPE and the host computer, and the calculations for searching neighbors in GRAPE. The above three orderings differ only in their data-transfer times. Figure 2 shows a corresponding plot for the isothermal density profile ($n = -2$), where the times for the GRAPE calculations without data transfer are also drawn as crosses. The differences between the crosses and the other marks indicate the times for data transfer and its overhead.

Generally, the consumption times show no clear difference among three density profiles, because GRAPE intrinsically does $O(N^2)$-operations, which do not depend on density profiles. Hence we hereafter discuss only the case for the density profile of an index $n = -2$. It is evident that M- and X-ordering work faster than R-ordering for any N, and that M-ordering is more efficient than X-ordering.

In our GRAPE system, M-ordering works twice as fast as R-ordering for $N = 10000$, while X-ordering does only 1.3 times as fast. M-ordering is 1.5 times faster than R-ordering for $N = 50000$, while X-ordering is 1.1 times faster. Both M- and X-ordering apparently become less effective for larger N on the basis of the total calculation time (figure 2), while M-ordering keeps its efficiency even in larger N (see subsection 5.2). This is because both orderings save only the communication costs, i.e. $O(N)$-operations, between GRAPE and the host computer. However, calculations in GRAPE, i.e. $O(N^2)$, become more dominant for larger N.

For $N = 100000$, the largest number in our tests, X-ordering becomes inefficient, i.e. consuming almost the same amount of time as R-ordering, while M-ordering is still 1.4-times faster than R-ordering. Therefore, M-ordering is best suited for neighbor searches with GRAPE.

5.2. *Data Compression Factor*

In section 2 we described how the communication time between GRAPE and a host computer is reduced if we make neighbor lists for 48 particles, kept in a memory unit in a single GRAPE run, overlap each other. In order to describe how much the lists overlap, we define the mean data compression factor of neighbor lists as

Table 1. Time consumed by neighbor search.

	Power index $n = 0.0$			Power index $n = -2.0$			Hernquist model		
Number	R-ord.	X-ord.	M-ord.	R-ord.	X-ord.	M-ord.	R-ord.	X-ord.	M-ord.
10000	0.61	0.45	0.30	0.60	0.45	0.30	0.55	0.40	0.28
20000	1.40	1.18	0.79	1.40	1.18	0.79	1.34	1.11	0.75
30000	2.41	2.17	1.48	2.52	2.23	1.49	2.36	2.09	1.42
40000	3.75	3.44	2.36	3.75	3.42	2.37	3.56	3.24	2.29
50000	5.07	4.75	3.43	5.09	4.73	3.43	4.95	4.58	3.33
60000	6.95	6.52	4.69	6.85	6.42	4.70	6.64	6.23	4.60
70000	8.89	8.38	6.17	8.69	8.22	6.16	8.49	8.23	6.05
80000	10.9	10.3	7.80	10.9	10.3	7.82	10.3	9.89	7.63
90000	13.1	12.5	9.62	13.1	12.5	9.66	12.5	12.0	9.42
100000	15.2	14.7	11.6	15.2	14.7	11.6	15.1	14.5	11.4

Note. Test calculations for a unit sphere with a density profile of $\rho \propto r^n$, and the Hernquist profile. The consumption time is presented in units of second. The particles are randomly distributed, and R-, X-, and M-ordering rearrange the particles in *random* order, in X-coordinate order, and in Morton order, respectively, before GRAPE calculations.

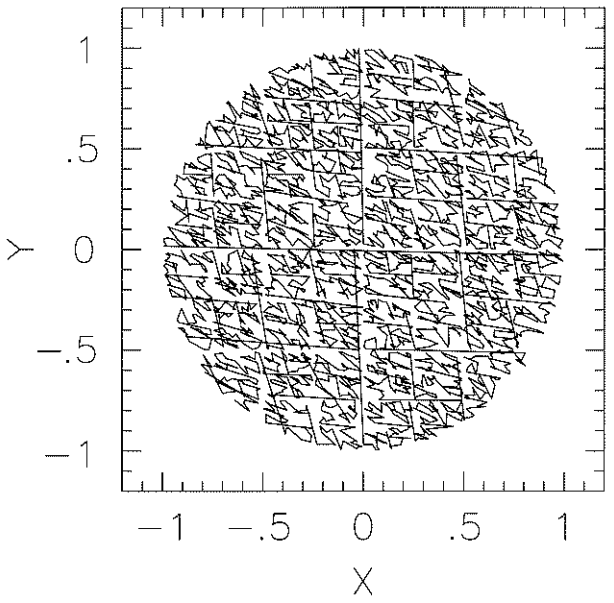

Fig. 1. Demonstration of the Morton ordering in a 2-D case for $N = 3000$. Randomly distributed particles are connected in a Morton order.

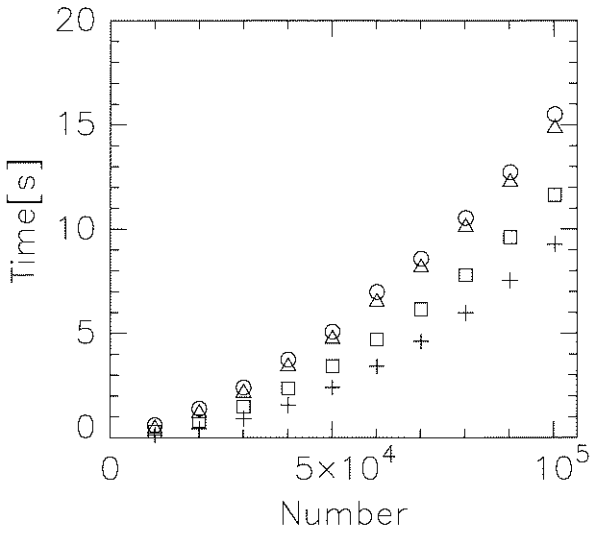

Fig. 2. Consumption time vs. number of particles, in the case for the density profile index of $n = -2$. The circles represent the times for R-ordering, the triangles are for X-ordering, and the squares are for M-ordering. The crosses indicate the time consumed for GRAPE calculations without any data transfer, which cannot intrinsically be suppressed in the above three methods.

$$f = \frac{N_{\rm b}^{\rm trans}}{N_{\rm b}^{\rm total}}, \tag{2}$$

where $N_{\rm b}^{\rm total}$ is a simple sum of the numbers of neighbors for all $n_{\rm p}$ particles, and $N_{\rm b}^{\rm trans}$ is the number of neighbors actually transferred from GRAPE to the host computer, according to the GRAPE specifications (section 2). We note that this factor does not depend on the speeds of a host computer and an interface between GRAPE and the host computer. The communication time is reduced in proportion to f.

If we consider a single GRAPE run and the case that each of the $n_{\rm p} = 48$ particles have 60 neighbors, $N_{\rm b}^{\rm total}$ is $48 \times 60 = 2880$. If the neighbors of the 48 particles are completely independent, $N_{\rm b}^{\rm trans}$ becomes $48 \times 60 = 2880$. Then, the compression factor becomes $f = 1$, meaning no compression. If the neighbor lists are perfectly identical, $N_{\rm b}^{\rm trans}$ becomes 60 as described in section 2, and then the compression factor takes its theoretical minimum, i.e. $f = 1/n_{\rm p}$ [note that this is an insubstantially ideal case (see appendix 2)]. For test calculations with a large number of particles, the GRAPE run must be repeated many times. Then, we average f in all of the data transfer for neighbor lists in all of the runs.

Table 2 lists f for all of the test calculations, and a corresponding plot for the isothermal profile ($n = -2$) is presented in figure 3. The compression factors f of R- and X-orderings increase with the number of particles, N. The f for X-ordering is efficiently as small as 0.5 for $N = 10000$; however, it increases to about 0.8 for $N = 100000$. R-ordering shows

Table 2. Data-compression rate f.

	Power index $n = 0.0$			Power index $n = -2.0$			Hernquist model		
Number	R-ord.	X-ord.	M-ord.	R-ord.	X-ord.	M-ord.	R-ord.	X-ord.	M-ord.
10000	0.85	0.48	0.12	0.85	0.47	0.13	0.85	0.47	0.13
20000	0.92	0.60	0.13	0.92	0.59	0.13	0.93	0.59	0.14
30000	0.95	0.67	0.13	0.95	0.66	0.13	0.95	0.65	0.14
40000	0.96	0.72	0.13	0.96	0.70	0.13	0.96	0.70	0.14
50000	0.97	0.75	0.13	0.97	0.73	0.13	0.97	0.73	0.14
60000	0.97	0.77	0.13	0.97	0.76	0.13	0.97	0.76	0.14
70000	0.98	0.78	0.13	0.98	0.77	0.13	0.98	0.77	0.14
80000	0.98	0.79	0.13	0.98	0.78	0.13	0.98	0.78	0.14
90000	0.98	0.81	0.13	0.98	0.79	0.13	0.98	0.79	0.14
100000	0.98	0.82	0.13	0.98	0.80	0.13	0.98	0.80	0.14

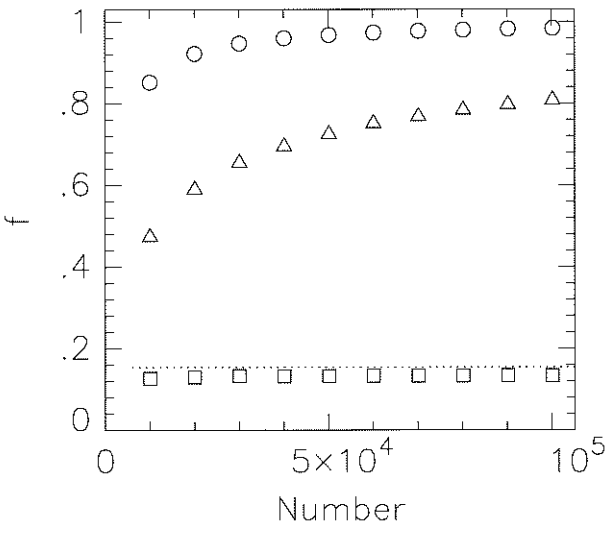

Fig. 3. Data-compression factor vs. number of particles, in the case for a density profile index of $n = -2$. The same marks are used as figure 2. The dotted line indicates a theoretical estimate of f in the case that the $n_p = 48$ particles are spherically distributed (see appendix 2).

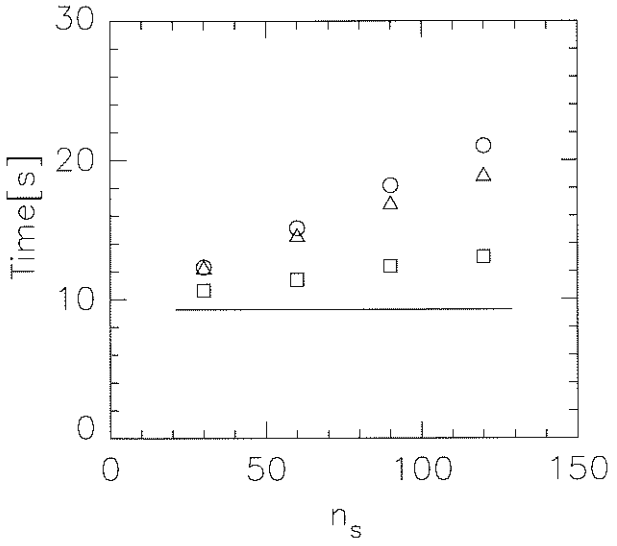

Fig. 4. n_s-dependence of the consumption time for $n = -2.0$ and $N = 100000$. The circles represent the times for R-ordering, the triangles for X-ordering, and the squares for M-ordering. The solid line indicates the consumption time for GRAPE calculations without data transfer.

almost no data compression ($f = 0.98$), that is, 98% are left for data transfer in the case of $N = 100000$. Hence X- and R-orderings do not work well for large N calculations. On the other hand, M-ordering keeps f almost constant at the low value of 0.13 for all Ns (figure 3). This is why M-ordering is still effective in large-N calculations. The low value of $f = 0.13$ means that the neighbor lists, sorted simultaneously on a single GRAPE memory unit, overlap almost perfectly (87%), and thus, implies that there is little room for further improvement. Therefore, we conclude that our new method (GRAPE+Morton ordering) is the best for neighbor searches using GRAPE.

5.3. *Dependence on n_s*

Figure 4 shows the n_s-dependence of the consumption time in the case of an isothermal density profile ($n = -2$) and $N = 100000$. We tested the range of $n_s = 30$–120, which is used in actual SPH calculations. Basically, the consumption times increase with n_s, because the number of neighbor particles, transferred from GRAPE to the host, increases with n_s. We note, however, that there is another effect that suppresses the increase of time. The larger n_s means larger radii (volumes) of particles, and thus, indicates larger overlap of their neighbor lists. This reduces data transfer, and results in saving time. Figure 5 shows this effect; the overlap fractions f decrease with increasing n_s. In our realistic range of n_s, M-ordering shows the best overlap fraction, and thus is the best for in any n_s.

6. Summary

We have reviewed the specifications of a special-purpose hardware called GRAPE, and introduced a new method which can speed up neighbor searches in large particle simulations

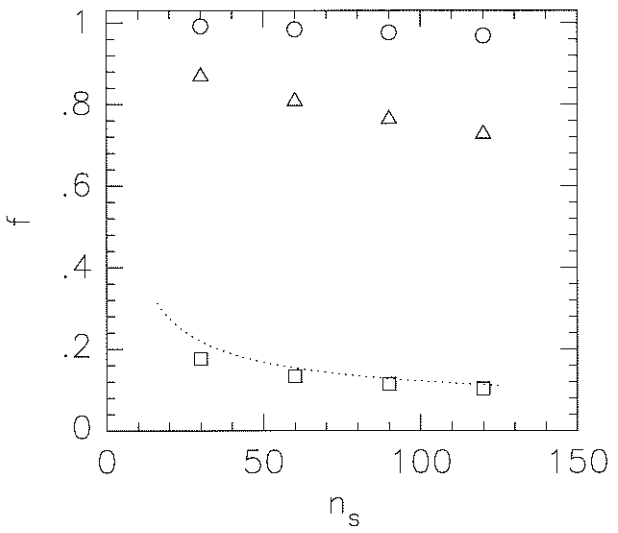

Fig. 5. n_s-dependence of the data-compression factor f for $n = -2.0$. The same marks are used as figure 4. The dotted line indicates a theoretical estimation of f in the case that the $n_p = 48$ particles are spherically distributed (see appendix 2).

using GRAPE. The main conclusions are the following:

1. We introduced a new method; that is, arranging particles in a Morton order before performing GRAPE calculations. This method saves the communication cost between GRAPE and its host computer. The cost for additional programming is very low.
2. We compared this Morton-ordering method with some previous methods, and concluded that the Morton-ordering method is much more effective. In a case where the total particle number is $N = 10000$, the Morton-ordering method is twice as fast as a simple neighbor search with GRAPE in our GRAPE system.
3. Communication between GRAPE and its host computer can be minimized if the neighbor lists, stored in a single GRAPE memory unit, overlap each other. The Morton-ordering method reduces the communication by about 90%, thus leaving little room for further improvement.
4. The Morton-ordering method becomes less effective for larger particle simulations, as do the other previous methods, because $O(N^2)$-calculations, other than data transfer, become dominant. However, it is still efficient for simulations with $N = 100000$.
5. The communication increases with the typical number of neighbor particles. The Morton-ordering method is the best for in any number that is usually used in SPH calculations.
6. We showed the efficiency of the Morton-ordering method only for GRAPE-5. However, it is also suitable for the other versions of GRAPE. In fact, this method has been effectively used for galaxy-formation simulations using GRAPE-3 (Koda et al. 2000a,b).

T.R.S. would like to thank Asao Habe for his encouragement, Takashi Okamoto and Tamon Suwa for many useful discussions about coding. We thank Jun Makino, the referee, for useful suggestions, which improved the appendices. T.R.S. was supported by the Sasakawa Scientific Research Grant from The Japan Science Society (14-096). J.K. was financially supported by the Japan Society for the Promotion of Science for Young Scientists. Numerical computations were carried out on the GRAPE system (project ID: g02a09) at the Astronomical Data Analysis Center of the National Astronomical Observatory of Japan, which is an inter-university research institute of astronomy operated by the Ministry of Education, Culture, Sports, Science and Technology.

Table 3. Timing constants for performance estimation.

Parameter	Constant (s)
c_h	1.8×10^{-5}
c_g	9.0×10^{-10}
c_t	7.3×10^{-7}

Appendix 1. Performance Estimation

The total calculation time for neighbor search with GRAPE is modeled as

$$T = T_h + T_g + T_t, \tag{A1}$$

where T_h, T_g, and T_t stand for the time consumed on the host computer, that on GRAPE, and that on data transfer of neighbor lists from GRAPE to the host computer, respectively. T_h and T_g are modeled as

$$T_h = c_h N, \tag{A2}$$

$$T_g = c_g N^2, \tag{A3}$$

where c_h and c_g represent the miscellaneous calculation time per particle on the host computer, and the time spent on a two-body interaction on GRAPE, respectively. N is the number of particles in the calculation.

The total number of neighbor particles transferred from GRAPE to the host computer is $Nn_s f$, where n_s is the typical number of neighbors for one particle, and f is the data-compression factor, defined in subsection 5.2. T_t would take the form

$$T_t = c_t N n_s f, \tag{A4}$$

where c_t is the time spent on data transfer per neighbor particle. For our GRAPE system (GRAPE-5 and a host computer with an Alpha 264 processor 833 MHz), we obtain the coefficients by fitting, and list them in table 3. Figure 6 shows a plot of estimated vs. measured T for R-, X-, and M-orderings. Different symbols are used for different orderings. All of the points are well on the proportional line (solid).

Appendix 2. Theoretical Estimate of f

The data-compression factor, f, takes the minimum of $1/n_p$ in an *insubstantially* ideal case that all the n_p particles have

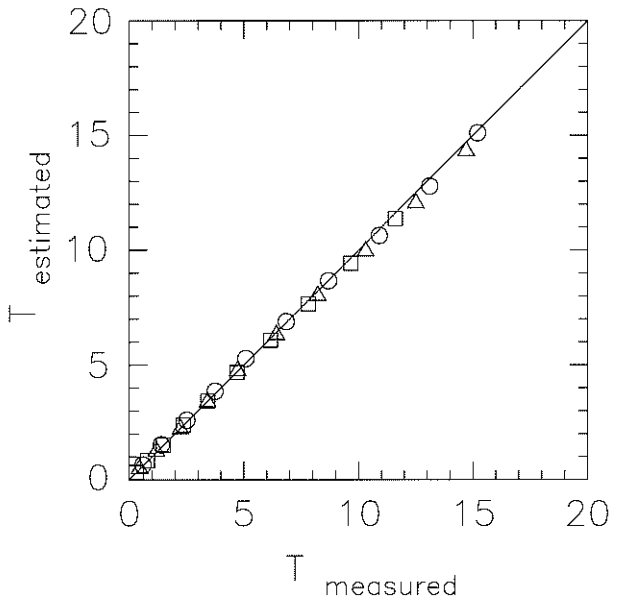

Fig. 6. Estimated vs. measured times consumed on neighbor search. The same marks are used as figure 4. The solid line is a proportional line. The estimated time is calculated by equation (A1).

an identical neighbor list; however, its actual minimum, which occurs in a calculation, would be larger. We estimate the f in a *thoughtfully* ideal case, and compare it with the results of M-ordering. We consider the case that the n_p particles (see section 2) are selected very successfully, i.e. the case that their neighbor lists overlap almost as much as possible. Since we have shown that f does not depend on the distribution of particles (section 5), we assume that N particles are distributed in a unit sphere with a uniform density, i.e. $\rho = 3N/4\pi$. In the ideal case, the n_p particles themselves must be closest neighbors each other, and be clustered in a small region. In the following we assume that this region has a spherical form.

The n_p particles are distributed in a sphere with a radius $r_p = (n_p/N)^{1/3}$. If we take into account that some of the n_p particles are on the surface of the sphere, and that each of them has n_s neighbors and a radius $r_s = (n_s/N)^{1/3}$, then all the neighbors of n_p particles will be *at least* within a sphere of the radius $r_a = r_p + r_s$. Hence, the number of neighbor particles, stored in a GRAPE memory and transferred from GRAPE to the host computer, becomes

$$N_b^{\rm trans} = (n_p^{1/3} + n_s^{1/3})^3. \tag{A5}$$

Since the total accumulated number of neighbors for the n_p particles is $N_b^{\rm total} = n_p n_s$, f is calculated as

$$f = \frac{(n_p^{1/3} + n_s^{1/3})^3}{n_p n_s}. \tag{A6}$$

This f does not depend on N, and approaches $1/n_p$ when $n_s \to \infty$. Figure 3 shows this f (dotted line). The results of M-ordering (squares) are close to the estimated f of this ideal case.

Note that we assumed here that all of the neighbors are closely packed in an even spherical space with a radius of $r_a = r_p + r_s$. However, this assumption is valid only in an infinite limit of n_s, because the actual space occupied by small n_s particles must have an uneven surface, which is completely enclosed by our assumed sphere. Thus, $N_b^{\rm trans}$ (and f) is smaller than that estimated by equation (A5). Hence, in figure 3, M-ordering gives a slightly smaller f than the estimated one for the spherical case. This difference becomes smaller with increasing n_s, which is confirmed in figure 5 (dotted line and squares).

Equation (A6) gives a thoughtful minimum of f that can occur in actual calculations. The fair coincidence of this minimum value with those from M-ordering gives us the confidence that M-ordering is an ideal method for neighbor search in GRAPE-SPH.

References

Barnes, J. E., & Hut, P. 1989, ApJS, 70, 389
Fukushige, T., & Makino, J. 1997, ApJ, 477, L9
Hernquist, L. 1990, ApJ, 356, 359
Ito, T., Ebisuzaki, T., Makino, J., & Sugimoto, D. 1991, PASJ, 43, 547
Ito, T., Makino, J., Ebisuzaki, T., & Sugimoto, D. 1990, Computer Physics Comm., 60, 187
Kawai, A., Fukushige, T., Makino, J., & Taiji, M. 2000, PASJ, 52, 659
Klessen, R. 1997, MNRAS, 292, 11
Koda, J., Sofue, Y., & Wada, K. 2000a, ApJ, 531, L17
Koda, J., Sofue, Y., & Wada, K. 2000b, ApJ, 532, 214
Kokubo, E., & Ida, S. 1998, Icarus, 131, 171
Makino, J. 1996 in IAU Symp. 174, Dynamical Evolution of Star Clusters, ed. P. Hut & J. Makino (Dordrecht: Kluwer), 151
Makino, J., & Ebisuzaki, T. 1996, ApJ, 465, 527
Makino, J., Taiji, M., Ebisuzaki, T., & Sugimoto, D. 1997, ApJ, 480, 432
Mori, M., Yoshii, Y., & Nomoto, K. 1999, ApJ, 511, 585
Okumura, S. K., et al. 1993, PASJ, 45, 329
Steinmetz, M. 1996, MNRAS, 278, 1005
Steinmetz, M., & Müller, E. 1995, MNRAS, 276, 549
Sugimoto, D., Chikada, Y., Makino, J., Ito, T., Ebisuzaki, T., & Umemura, M. 1990, Nature, 345, 33
Umemura, M., Fukushige, T., Makino, J., Ebisuzaki, T., Sugimoto, D., Turner, E. L., & Loeb, A. 1993, PASJ, 45, 311
Warren, M. S., & Salmon, J. K. 1995, Computer Physics Comm., 87, 266
Weil, M. L., Eke, V. R., & Efstathiou, G. 1998, MNRAS, 300, 773